

Topological shape transform for thymus structures

Haochen Yang^{1,2,3,4}, Vadim Lebovici⁶, Andreas Tarcewski⁷, Liliana Tchernev^{7,9}, Saulius Zuklys⁸,
Georg A. Holländer^{*7,8,9,10}, Helen M. Byrne^{†1,2}, and Heather A. Harrington^{‡1,3,4,5}

¹Mathematical Institute, University of Oxford, Oxford OX2 6GG, United Kingdom

²Ludwig Institute for Cancer Research, Nuffield Department of Medicine, Oxford OX3 7DQ, United Kingdom

³Centre for Systems Biology Dresden, Dresden 01307, Germany

⁴Max Planck Institute of Molecular Cell Biology and Genetics, Dresden 01307, Germany

⁵Technische Universität Dresden, Dresden 01062, Germany

⁶Sorbonne University, Institut de Mathématiques de Jussieu-Paris Rive Gauche, Paris 75005, France

⁷Department of Paediatrics, University of Oxford, Oxford OX3 9DU, United Kingdom

⁸Paediatric Immunology, Department of Biomedicine, University of Basel, Basel 4058, Switzerland

⁹Botnar Institute of Immune Engineering, Basel 4052, Switzerland

¹⁰Department of Biosystems Science and Engineering, ETH Zurich, Basel 4056, Switzerland

Abstract

The Euler characteristic transform (ECT) is an emerging and powerful framework within topological data analysis for quantifying the geometry of shape. The applicability of ECT has been limited due to its sensitivity to noisy data. Here, we introduce SampEuler, a novel ECT-based shape descriptor designed to achieve enhanced robustness to perturbations. We provide a theoretical analysis establishing the stability of SampEuler and validate these properties empirically through pairwise similarity analyses on a benchmark dataset and showcase it on a thymus dataset. The thymus is a primary lymphoid organ that is essential for the maturation and selection of self-tolerant T cells, and within the thymus, thymic epithelial cells are organized in complex three-dimensional architectures, yet the principles governing their formation, functional organization, and remodeling during age-related involution remain poorly understood. Addressing these questions requires robust and informative shape descriptors capable of capturing subtle architectural changes across developmental stages. We develop and apply SampEuler to a newly generated two-dimensional imaging dataset of mouse thymi spanning multiple age groups, where SampEuler outperforms both persistent homology-based methods and deep learning models in detecting subtle, localized morphological differences associated with aging. To facilitate interpretation, we develop a vectorization and visualization framework for Sam-

pEuler, which preserves rich morphological information and enables identification of structural features that distinguish thymi across age groups. Collectively, our results demonstrate that SampEuler provides a robust and interpretable approach for quantifying thymic architecture and reveals age-dependent structural changes that offer new insights into thymic organization and involution.

Keywords: topological data analysis | Euler characteristic transform | thymus | involution | geometric morphometrics

Introduction

Morphological information has proven invaluable for understanding how structure relates to function in biological tissues, organs, and organisms [1, 2, 3]. Identifying and quantifying distinct shapes are central tasks in biology since geometric differences can indicate variations in developmental processes, disease states, or differences in biological function. The thymus is an essential organ of the adaptive immune system responsible for the maturation, selection, and differentiation of T cells [4]. Within the confines of the thymic microenvironment, T cells are instructed by thymic epithelial cells (TECs) and other stroma cells to establish a diverse, yet self-tolerant T cell receptor (TCR) repertoire - a process known as thymopoiesis [5]. With age, the thymus undergoes involution characterized by reduced total cell numbers, disruption of the epithelial network architecture, and diminished naive T cell output [6, 7]. Paralleling thymic involution and reduced thymopoietic activity, the TCR repertoire becomes constricted with age [8]. Together, this leads to an increased susceptibility

*To whom correspondence should be addressed. E-mail: georg.hollander@paediatrics.ox.ac.uk

†Corresponding author. E-mail: helen.byrne@maths.ox.ac.uk

‡Corresponding author. E-mail: Harrington@mpi-cbg.de

to viral infections, heightened autoimmunity, and diminished surveillance of malignant cells due to the immune system’s diminishing capacity to mount effective responses to de-novo antigens [9, 10, 11]. Simultaneously, the thymus undergoes significant architectural remodeling, with both cortical TECs (cTECs) and medullary TECs (mTECs) exhibiting structural changes [2, 12]. To better understand these changes, precise mathematical descriptors are needed to quantify morphological changes at the cell level. A variety of shape descriptors have been developed for biological structures, ranging from deep learning frameworks that leverage large datasets to automatically learn shape representations [13], to techniques grounded in differential geometry that focus on curvature and other geometric invariants [14].

Recent advances in topological data analysis (TDA), a field dedicated to extracting geometric and topological insights from spatial data, have led to the introduction of persistent homology [15, 16] and to the development of the Euler Characteristic Transform (ECT) [17]. Extensions to ECT and refined transforms have been devised to capture aspects of shape analysis [18, 19, 20], and theoretical studies have established important properties of the ECT, including its invertibility [21, 22, 23] and the existence of stability bounds [24, 25]. The invertibility of ECT means that it captures all geometric and topological information of the input shape and is highly effective at capturing morphological differences between shapes. Despite the stability results, the ECT remains extremely sensitive to small perturbations and misalignments in the input shape, undermining its practical robustness. Although several alignment procedures have been proposed to address these issues [26, 27, 19], they often come at a high computational cost. Recent theoretical advances [22] have effectively resolved the sensitivity to misalignments, but the isometry invariant algorithms they have inspired [28] suffer from unsatisfactory levels of information loss.

Motivated by the limitations of existing isometry invariant algorithms, we introduce SampEuler, a discrete construction based on the ECT, which comes with theoretical guarantees about the information it captures and its stability. Building on SampEuler, we introduce a vectorization and visualization algorithm for the ECT. We first apply SampEuler and its vectorization to synthetic tree structures and show that they outperform current topological shape transforms. We then benchmark against conventional shape analysis methods and TDA methods using the MPEG7 dataset.

Finally, we apply SampEuler to a dataset of equally sized quadrants, extracted from binary images of mouse thymi across different age groups, to characterize age-related structural changes. In our classification study, we benchmark our methods against state-of-the-art TDA, including various vectorizations of persistent homology, as well as deep learning methods, demonstrating that Sam-

pEuler achieves higher classification accuracy in significantly less computation time. We interpret the classification results based on the vectorization of SampEuler in relation to underlying thymic structural differences, thereby providing valuable biological insights. Moreover, we compare the analysis of these quadrants based on shape descriptors with T-cell distribution analysis to study the relationship between the impact of ageing on T-cell distribution and thymic architecture.

Description of Datasets

We evaluate SampEuler on three datasets: synthetic structures for the method validation, established shape benchmarks for comparison with existing approaches, and mouse thymus images for biological applications.

Synthetic Networks

We produce simple geometric simplicial complex examples as networks consisting of three edges of fixed lengths emanating from a common origin that are uniformly discretized into points connected by edges in order. We perturb the points and the edges that connect them by adding Gaussian noise. This creates a controlled setting within which to evaluate the performance of ECT-based methods under perfect alignment versus rotational perturbations. Two representations of two groups of simplices are shown in Figure 1A. Details of the dataset can be found in the *SI Appendix*.

MPEG-7 Shape Library

We use the published image dataset from previous shape descriptor studies [29, 30, 31, 32, 33, 34, 17, 28, 35, 36, 37, 38]. The dataset consists of 70 groups of 2D binary images, each group containing silhouettes of objects from the same category. For example, one group contains 20 images of horse silhouettes. Although all the underlying objects are horses and share similar geometry, they are not identical; in many cases, a 2D isometry—such as a slight rotation—is applied to the object before the image is captured so that the same side of the horse is photographed from different angles.

We preprocess the dataset by first padding each image with black pixels to achieve a consistent size of 1126 pixels \times 1126 pixels. Next, we denoise the images by retaining only the largest connected component of white pixels—treating any additional white pixels as false positives and converting them to black. The processed images are then used for further analysis. The preprocessing details are included in the *SI Appendix*.

Mouse Thymus Dataset

Mouse thymi (n=7) were processed as described in ‘Materials and Methods’ (see below). The boundaries of the thymic epithelial cell (TEC) network were segmented using MATLAB’s Image Processing Toolbox: multilevel thresholding (`multithresh`) and skeletonization (`bwskel`) were applied to the cytokeratin 8 (K8) and cytokeratin 14 (K14) TEC markers to generate 2D binary images for all 7 thymi and both markers (values of 1 where the K8/K14 staining is present, 0 where it is absent). A 200 x 200 pixel lattice was superimposed on the 2D images to generate subimages, for subsequent TDA.

Results

We introduce SampEuler to capture shape information in a way that is robust to noise and overcomes the sensitivity of ECT (Figure 1). We show that the proposed approach achieves higher accuracy with less computational cost than existing methods, including persistent homology vectorizations, ECT-based approaches, and deep learning models (Figure 2). Employing SampEuler on the images of mouse thymi, we achieve age classification based on the shape of local thymic structures (Figure 3). Comparing with the distribution of T cells, we identify relationships between thymic structure and cellular composition at different ages (Figure 4).

From Data to Topological Transforms

Within TDA, the ECT is an integral transform that has been extended in numerous ways and successfully applied to biological datasets [18, 20, 27, 39, 19]. Such data comes in the form of n-dimensional images or discretized boundaries of segmented structures; these can be represented as simplicial complexes comprising points, edges, faces, and higher-dimensional simplices. One of the simplest computable topological invariants, the Euler characteristic, is given by the alternating sum of the number of n-dimensional simplices in the simplicial complex K : $\chi(K) = \sum_{i=1}^n (-1)^i \#$ of i dimensional simplices in K , where n is the maximal dimension of all simplices in K . To capture geometric information of the complex, Turner et al. proposed sweeping a (hyper)plane through the shape progressively in time (t) in a given direction (v) and computing the Euler characteristic (χ), which outputs an integer-valued curve for the particular direction (Equation (0.1)). By sweeping through all directions, the Euler characteristic transform (ECT) is the correspondence between directions and curves (Equation (0.2)). The ECT is invertible, meaning one can reconstruct the original shape and thereby derive any geometric information captured by other shape descriptors [21, 22, 23].

$$\text{ECC}_K^v : \mathbb{R} \rightarrow \mathbb{Z}; t \mapsto \chi(K \cap \{x \in \mathbb{R}^n : x \cdot v \leq t\}). \quad (0.1)$$

$$\text{ECT}(K) : S^{n-1} \times \mathbb{R} \rightarrow \mathbb{Z}; (v, t) \mapsto \text{ECC}_K^v(t). \quad (0.2)$$

Since the ECT is sensitive to the complex, DETECT ([28]) was proposed to smooth, normalize, and average across all ECC_K^v :

$$\text{DETECT}(K) : [-a, a] \rightarrow \mathbb{R}; \quad (0.3)$$

$$c \mapsto \int_{S^{n-1}} \left(\int_{-a}^c \text{ECC}_K^v(t) - \left(\frac{1}{2a} \int_{-a}^a \text{ECC}_K^v(s) ds \right) dt \right) dv \quad (0.4)$$

We apply ECT and DETECT to the synthetic networks. To visualize the discriminative power of each method, we embed the resulting shape descriptors in two dimensions using multidimensional scaling (MDS) [40, 41]. The standard ECT distinguishes two classes of perfectly aligned shapes, whereas DETECT fails (Figure 1B-C, left), illustrating the information loss introduced during the averaging step. Indeed, both complexes yield identical DETECT transforms.

When the shapes are perturbed randomly to simulate the misalignment in applications, both methods fail to distinguish the two classes of complexes (Figure 1B-C, right).

Introduction to SampEuler

To overcome the sensitivity of ECT to perturbations on input shapes and the information loss of DETECT, we propose to record only the output curves and not the direction v in ECC. This shape transform is isometry-invariant. To achieve this mathematically, we consider the ECT pushforward measure of K , which can be thought of as the probability law of ECCs of K for a given direction chosen uniformly at random. The ECT pushforward measure is proven to be injective up to rotations and reflections [22].

By convention, the shape of a given complex is the equivalence class of the complex up to rotations, reflections, and translations. We centre all complexes by translating their barycentres to the origin to filter the translation information. On these centred complexes, the ECT pushforward measure serves as a complete shape descriptor: two complexes have the same ECT pushforward measure if and only if they have the same shape. The ECT pushforward measure is a probability law on the function space; and therefore is hard to compute in practice. Based on the ECT pushforward measure, we propose an isometry-invariant shape descriptor, **SampEuler**. SampEuler samples curves from the ECT pushforward measure and outputs an empirical measure formed by the sampled curves. We show that the SampEuler converges to the ECT pushforward measure as the discretization is refined. Equipped with the Wasserstein distance [42], it induces a continuous map from the input complex to its SampEuler representation. We also introduce a vectorization and visualization method for SampEuler. For small datasets, the vectorized representation yields a low-dimensional feature space that supports effective training of standard machine-learning models and, when paired with interpretation techniques, allows

direct geometric interpretation. For larger or geometrically complex datasets, using the full SampEuler representation preserves complete geometric information with theoretical guarantees, avoiding information loss from dimensionality reduction. Details and proofs of SampEuler convergence and continuity are included in the *SI Appendix*.

We apply SampEuler and its vectorization to the synthetic networks, visualizing the results using MDS (Figure 1D-E). In both cases, SampEuler and its vectorization correctly distinguish the two classes (see *SI Appendix* for more details), demonstrating that they are both isometry invariant and informative.

SampEuler Outperforms Topological Statistics

We apply SampEuler and its vectorization with Support Vector Machine (SVM) to classify the MPEG-7 dataset and benchmark against other methods. Details of image preprocessing and the experiments can be found in Materials and Methods.

We benchmark SampEuler against standard TDA methods that use the 10-class subset of MPEG-7: Persistence Scale Space Kernel [29], Persistence Weighted Gaussian Kernel [30], Sliced Wasserstein Kernel [31], Tangent Vector Representation with Gaussian Kernel [32], Persistence Fisher Kernel [33], and QUPID [34]. As shown in Figure 2B, SampEuler outperforms conventional TDA methods.

We run the classification task over the whole MPEG7 dataset to compare with other methods (Figure 2): Skeleton Paths [35], Bag of Contours [36], Persistence Image + Neural Network (PI+NN) [37], Persistence Codebook + Neural Network (PC+NN) [38]. SampEuler and its vectorization exhibit consistent performance; however, they are outperformed by dedicated 2D image recognition algorithms and TDA with deep learning approaches. We remark that topological methods offer more interpretability than deep learning, whose decision processes can be comparatively opaque.

To understand the effect of discretizing ECT and ECT pushforward in practice, we use the MPEG-7 dataset and vary the number of filtration values sampled along each curve and the total number of curves sampled, and perform classification tasks with SVM. Experimental details and full results can be found in *SI Appendix*. We report that if we sample more than 100 directions and 1000 points along each direction, we obtain high accuracy, and the additional information obtained for the MPEG7 dataset is limited. Moreover, leveraging the optimised implementation in Eucalc [45] enables efficient computation of these descriptors, making the above parameter choices practical in routine use.

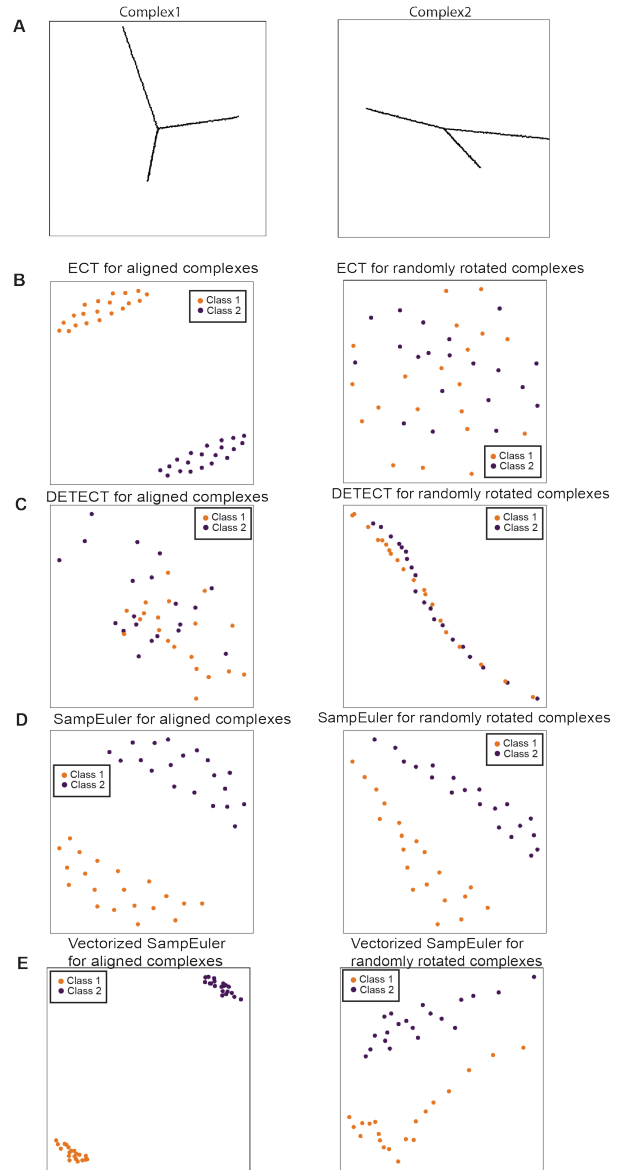


Figure 1: MOTIVATION FOR NEW PUSHFORWARD MEASURE on ECT. We apply ECT, DETECT, SampEuler, and vectorization of SampEuler to aligned to simplicial complexes (Left) and randomly rotated simplicial complexes (right). (A) Representations of simplicial complexes from the two classes. Each class shares the same base complex, in other words, the same shape, generated by attaching one end of three edges of fixed lengths with 100 vertices along each edge. We attach one end to the origin and randomly rotate the other end around the origin. For each sample, we add Gaussian noise at points along each edge. In the aligned case, we use the resulting complexes directly. In the rotated case, we apply individual random rotations centred at the origin to the whole complex around the origin. (B) Two-dimensional MDS embedding (a projection that preserves pairwise distances between shapes) of ECT shape descriptors. The results of two distinct classes can be separated when all complexes are aligned. However, in the rotated case, ECT results are heavily affected by the rotations and fail to distinguish two classes. (C) MDS embedding of DETECT shape descriptors. DETECT fails to distinguish two classes of shapes in both experiments due to information loss. (D) MDS embedding of SampEuler shape descriptors. In both experiments, the two classes

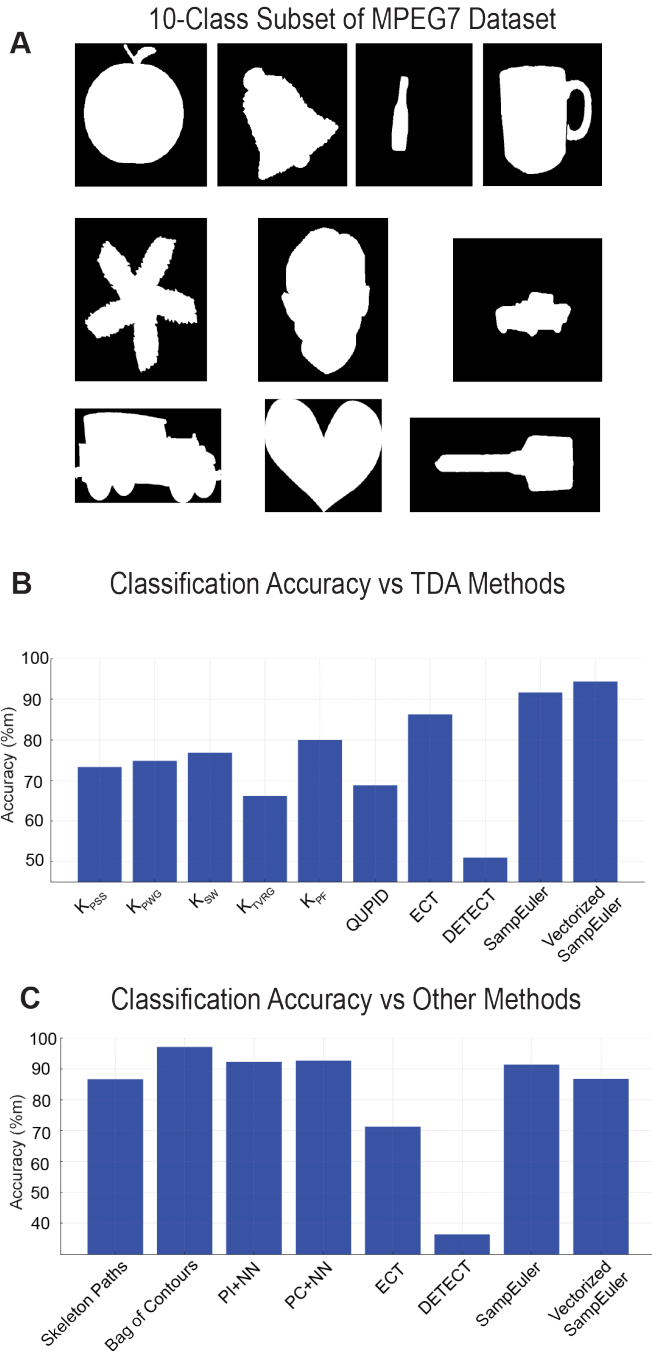


Figure 2: CLASSIFICATION STUDY on MPEG7 DATASET. We compare SampEuler with conventional shape analysis methods using the MPEG7 dataset [43]. (A) Examples of the MPEG7 dataset images, one sample from each of the 10-class subset used in previous studies [33, 44]. (B) The barplot of the accuracy of each method in the classification task of the 10-class subset of MPEG7. We denote Persistence Scale Space Kernel [29] by K_{PSS} , Persistence Weighted Gaussian Kernel [30] by K_{PWG} , Sliced Wasserstein Kernel [31] by K_{SW} , Tangent Vector Representation with Gaussian Kernel [32] by K_{TVGR} , Persistence Fisher Kernel [33] by K_{PF} . (C) The barplot of the accuracy of each method in the classification task of the whole MPEG7 dataset (70 classes). We use methods: Skeleton Paths [35], Bag of Contours [36], Persistence Image + Neural Network (PI+NN) [37], Persistence Codebook + Neural Network (PC+NN) [38], ECT, DETECT, SampEuler and vectorization of SampEuler.

SampEuler Quantifies Ageing Impact on Thymic Structure

To assess how ageing affects local architecture of TEC, we sub-sampled quadrants of size 200×200 pixels in representative areas of the cortex (i.e. K8 segmentation mask) and medulla (K14 segmentation mask). We sampled 20 quadrants per thymic lobe, resulting in a total of 40 quadrants for young and 100 for old. They were used as input to a supervised, binary classification of young versus old (Figure 3A). For this resolution, we compute 360 directions and 300 points along each direction for all ECT-based methods.

We benchmark our proposed methods against the Persistence image [37] with the signed distance function, AlexNet [46], Visual Transformer [47], MobileNet V2 [48], EfficientNetB0 [49], ECT and DETECT to verify that they accurately quantify local thymic structure. Details of the experiments can be found in *SI Appendix*. The results are shown in Figure 3B-C. SampEuler and its vectorization give better accuracy with shorter run times, demonstrating their ability to efficiently detect age-related structural differences within the cortex or medulla.

To interpret geometric differences between age groups, we use the vectorization of SampEuler to visualize Euler characteristic curves across all directions. We apply the SHAP algorithm to identify which regions of this image are most important for classifying each age group. We repeat training 50 times, retaining trials with accuracy above 50% as valid. For each age group, we average SHAP values across test samples from all valid trials to obtain a final feature importance map (Figure 3D). These maps reveal the distribution of Euler characteristic curves that the classifier recognizes as typical for each age group: regions of high importance indicate where curves consistently lie, effectively summarizing each group’s typical shape signature.

In the cortical region (K8) of the thymus, both age groups exhibit an initial increase in Euler characteristic with increasing filtration value t , with a slightly steeper rise in young thymi. At higher values of t , older thymi show a markedly steeper decline in Euler characteristic and reach a lower minimum, whereas younger thymi decrease more gradually. Since the Euler characteristic for the images is computed from their corresponding 2D cubical complexes, we have that

$$\text{Euler characteristic} = \#(\text{connected components}) - \#(\text{loops}).$$

Here, the number of loops means the dimension of the first homology group of the cubical complex or, intuitively, the number of holes in the image. Using this relationship, we interpret the observed differences as follows: the steeper initial increase in young thymi suggests a higher density of connected components; the lower final Euler characteristic in older thymi indicates more loops in the cortical structure; and the steeper decline in older thymi implies these loops are more densely distributed.

In the medulla (K14) of the thymus, the major trends of both age groups are similar. However, we observe greater variation in the geometry of old thymi compared to young thymi. Old quadrants show more diverse patterns in their Euler characteristic curves, with a higher proportion exhibiting increased numbers of connected components. In particular, we use other methods to confirm these interpretations (see *SI Appendix*).

We also analyzed how morphological and cellular composition differences between age groups vary with cortical depth (Figure 3E). For each thymus, we defined a depth kernel ranging from 0 at the outer capsule to 1 at the cortico-medullary junction (CMJ). At each depth, we used energy distance [50] to quantify differences between age groups based on pairwise SampEuler distances (capturing structural differences) and T-cell enrichment ratios (capturing cellular composition across whole tiles; see *SI Appendix* for definitions). The results show that both morphological and cellular differences between age groups occur near the capsule and diminish towards the CMJ, highlighting coincident changes between cTEC morphology and cellular composition with age.

Comparing Cell Distribution with Shape

In addition to TEC segmentation, we annotated the hematopoietic and stromal cell types for this dataset. To compare the impact of ageing on both cell distributions and TEC architecture, we perform k-medoids clustering [51] separately based on cell enrichment ratios (see *SI Appendix* for definitions) and SampEulers.

Age-related thymic involution impacts medullary and cortical TEC types differentially. While both cell populations decrease in absolute terms, the relative representation of cTEC to mTEC increases with age [7]. cTECs are known to mediate key biological processes like lineage commitment and positive T cell selection [52]. These processes are essential for hematopoietic T cell precursors to a) adopt a T cell lineage, and later in development to b) probe their ability to bind self-peptide on MHC molecules. Therefore, we decided to focus on the cortical region for the subsequent analyses and investigate morphological changes in the cortical region along with compositional changes in proximal, abundant hematopoietic cell types. For the composition definition we limited this analysis to the most abundant and biologically informative hematopoietic cell types in the cortical compartment: double-negative type 3 (DN3) T cells, pre (positive) selection double-positive T cells (Presel DP), post (positive) selection double positive T cells (CD69-) (Postsel DP, CD69-), and post (positive) selection double positive T cells (CD69+) (Postsel DP, CD69+). Full phenotype marker definitions are provided in *SI Appendix*. Furthermore, we restricted the compositional analysis to those thymocytes that lie within $5\mu\text{m}$ distance to the K8 segmentation mask. We clustered all cortical quadrants from both age groups together so that cluster labels are

comparable across age.

To allow faster computation of the pairwise Wasserstein distance matrix of all cortex quadrants, we use the sliced Wasserstein distance algorithm [53] with 50 slices to approximate the true Wasserstein distance.

We first used the silhouette analysis [54] to find the best k for each clustering. The results suggest a maximal cluster purity at 2 clusters for both the shape and the cell composition based clustering. In practice, 2-medoid results do not provide sufficient biological granularity so we fixed $k = 3$ in both the SampEuler and the cell enrichment ratio-based clustering (Figure 4A). To complement the cell enrichment based clustering we calculated the average cell type enrichment ratios for key cortical cell types (Figure 4B). We observe that the overall spatial arrangement of the shape-clustering is largely preserved with age (Figure 4A i and iii), but this does not hold for the cell enrichment-based clustering. To quantify this observation, we computed the proportion of shape clusters within each cell enrichment ratio cluster separately for each age group (Figure 4C). The confusion matrices reveal that for the young tissue, the shape and the cell enrichment ratio-based clustering shows overlap, with higher intensity concentrated along the diagonal (Figure 4C i). For the old tissue, however, the cell enrichment clusters representing the sub-capsular, deep cortical, and cortico-medullary areas (Figure 4A iv) all show preferential association with shape cluster 2 (Figure 4A iii). To confirm this observation, we selected CD4 and CD8 double-negative, type 3 thymocytes (DN3s; a cell type that in young thymi is typically associated with the sub-capsular localization; *SI Appendix*, Fig. S13A) and investigated whether there is a significant shift of that population into the deeper cortex with age. Qualitatively, the DN3 population in old thymi appears to be more diffuse and less confined to the sub-capsular area than in young (*SI Appendix*, Fig. 13B). To see if this qualitative difference is significant, we computed the distances between the capsule and all DN3 centroids within a $500\mu\text{m}$ (sub-capsular) range for all samples (examples shown in *SI Appendix*, Fig. 13C). Then, we compared the resulting distributions of cell distances using a two-sample t-test ($p = 6.3\text{e-}11$) and a Wilcoxon test ($p = 3.1\text{e-}18$). These significantly different distributions indicate that DN3s in older thymi are less tightly localized to the sub-capsular region, suggesting that location-specific cellular organization in the sub-capsular region is disrupted with age.

Discussion

In this paper, we introduced and implemented SampEuler and its vectorization as two novel topological shape descriptors. We applied them to a benchmarking shape image dataset and a mouse thymus dataset. The results show that both novel shape descriptors are robust to rigid transformations, resolving the high sensitivity issue of ECT [17].

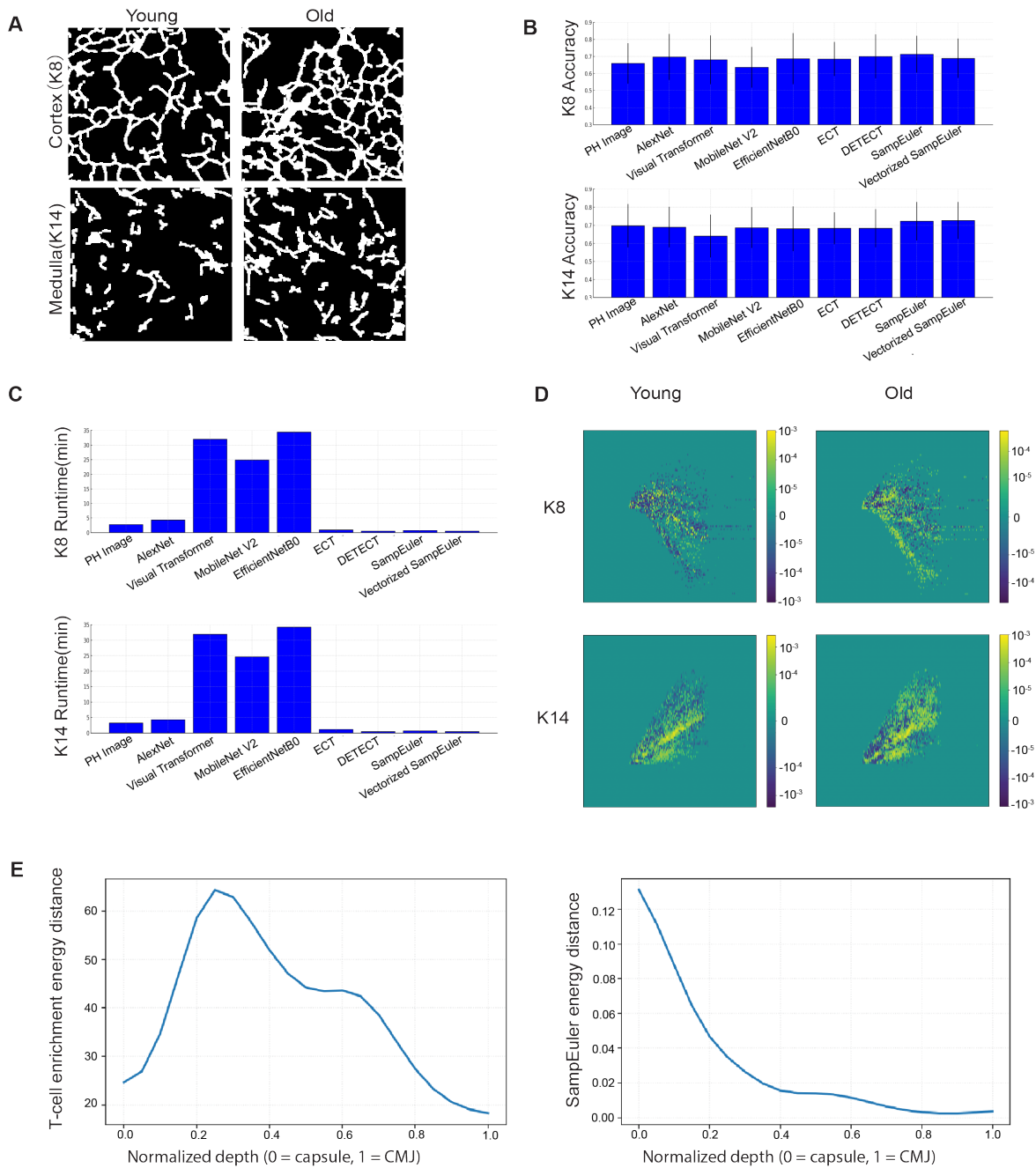


Figure 3: CLASSIFICATION STUDY ON SELECTED THYMIC QUADRANTS. We segment masked images of thymic epithelium into quadrants of size 200×200 pixels. Then, we classify them into old and young groups separately for K8 and K14 markers. (A) Example images of thymic quadrants of each age group and each marker. (B) Barplots of the classification accuracies of each method. The top plot contains accuracies for classifying K8 quadrants, and the bottom plot contains accuracies for classifying K14 quadrants. The error bars show the standard deviations for repeating the classification 50 times. (C) Barplots of the classification runtimes of each method. The top plot contains runtimes in minutes for classifying K8 quadrants, and the bottom plot contains runtimes in minutes for classifying K14 quadrants. (D) We use the SampEuler vectorization as input features for classification training. We repeat the train-test process 50 times and keep trials with over 80% accuracy. For trials with accuracy over 80%, we compute the SHAP value for each feature. For each marker and age group, we average across all test samples of the age group and then across all valid trials. The plot shows average SHAP values for each feature as feature importances towards classifying the sample as a given age group. (E) Depth-dependent comparisons between thymic quadrants from different age groups. For both plots, the x-axis shows the normalized depth of the thymus, where 0 corresponds to quadrants at the capsule and 1 to quadrants at the cortex–medulla junction (CMJ). In the left plot, the y-axis shows the energy distance [50] between age groups based on T-cell enrichment ratios. In the right plot, the y-axis shows the energy distance between age groups based on pairwise SampEuler distances.

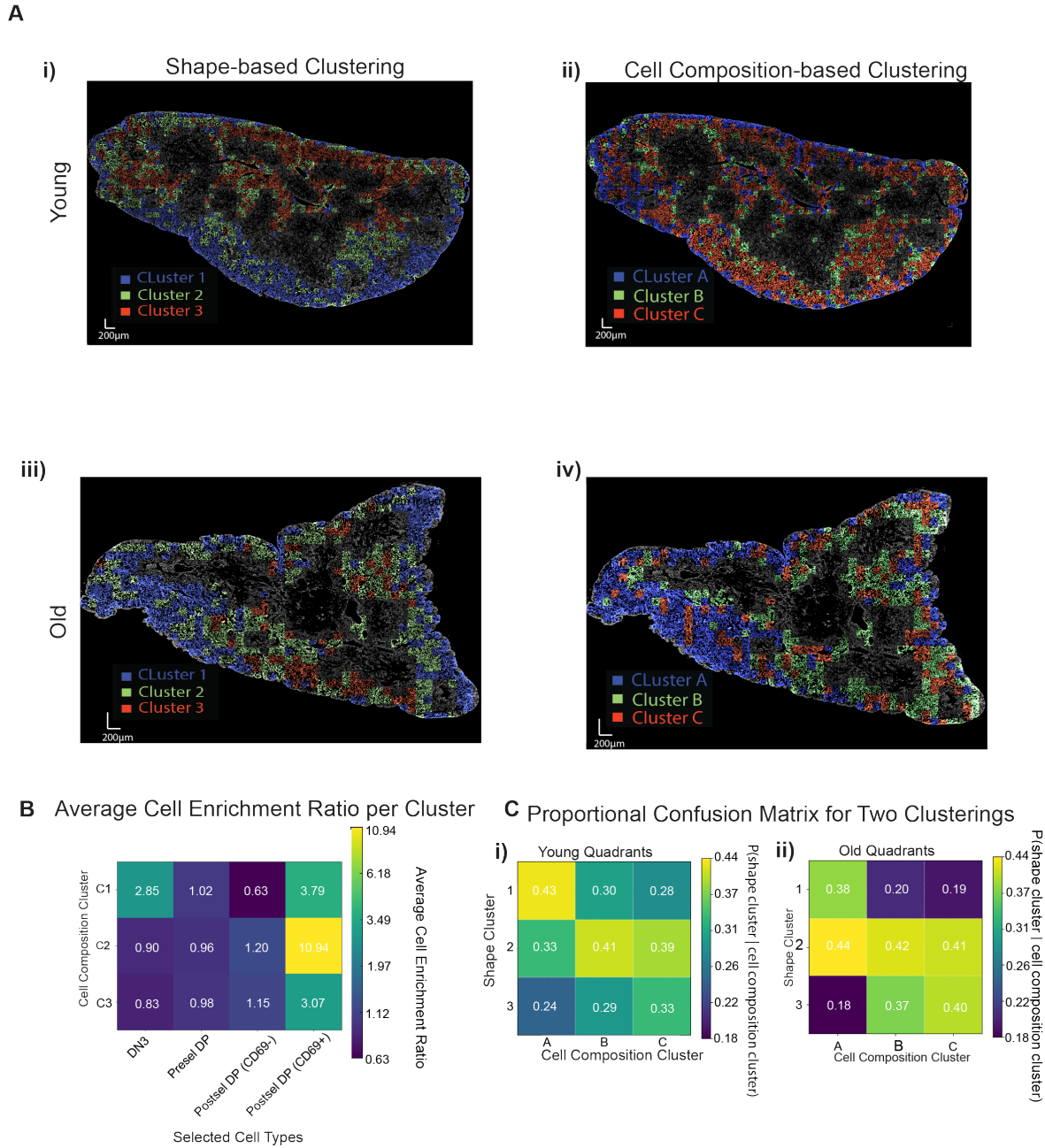


Figure 4: K-MEDOIDS CLUSTERING RESULTS. We cluster all cortex quadrants from both age groups using SampEuler distances and selected cell enrichment ratio distances with k-medoids clustering. We match the clustering results by finding the label permutation that gives the largest number of matched patches. (A) Example overlay images of the thymic quadrants. The top two samples are young thymi, and the bottom two samples are old thymi. A i) and iii) use SampEuler distances to perform shape-based clustering, and A ii) and iv) use selected cell type enrichment ratios. We permute the labels to obtain the best match between two results. (B) Average cell enrichment ratios by cluster and cell type. Rows represent the three cell-composition-based clusters, columns represent selected cell types, and values show the mean enrichment ratio for each cell type within each cluster. (C) Proportional confusion matrices of matching the two clustering results. The (i, j) -th entry of the matrix is given by the formula $\frac{\text{No. of quadrants being classified as shape cluster } i \text{ and cell composition cluster } j}{\text{No. of quadrants being classified as cell composition cluster } j}$

Moreover, SampEuler can extract shape information effectively to resolve subtle shape differences with high accuracy.

We demonstrated the effectiveness of SampEuler and its vectorization on synthetic three-edge tree simplices, highlighting their capacity to capture and emphasize purely shape-based information. Benchmarking on the MPEG7 dataset confirmed that SampEuler achieves higher classification accuracy than conventional TDA methods based on persistent homology. While dedicated 2D image recognition algorithms and TDA with deep learning approaches achieve higher accuracy, SampEuler provides a favorable balance between performance and interpretability. Their application to the mouse thymus dataset underscored the strength of SampEuler in the study of complex biological structures. The random forest classifiers trained on SampEuler and the vectorization of SampEuler achieved competitive accuracies ($> 70\%$) for age classification relying on a limited set of training data (i.e. cell shapes) at notably lower computational cost than deep learning models. This shows that a) a quantifiable change in cell morphology occurs with age for both cTEC and mTEC and b) this shape change can inform the age-category of the underlying sample. While this holds true for the two ages considered, a more granular approach (extending over more time points) is required to confirm its validity across a broader life trajectory. Applying the SHAP algorithm to random forest classifiers trained on SampEuler vectorizations enabled a mathematical characterization of cell shape. Although classification reveals detectable shape differences between age groups, these age-related changes appear to affect different morphological subtypes in parallel: each shape cluster undergoes its own characteristic shift with age, but the relative distinctions between clusters are preserved. Consequently, the overall spatial organization of shape clusters remains largely intact (Figure 4A i and iii). However, when considering cell composition clustering, a spatial shift becomes apparent with age. In young thymi, Cluster A is confined to the sub-capsular region, whereas in old thymi, this same compositional pattern extends deep into the cortical compartment (Figure 4A ii vs. iv). This spatial reorganization could arise from several age-related factors, such as loss of intra-thymic cytokine gradients that normally maintain youthful regional organization, or failure in the provision of lympho-stromal cross-talk necessary for double-negative T cell progression. However, additional experimental validation is required to confirm these hypotheses.

Building on these positive findings, we propose that future work investigate the theoretical properties of the ECT pushforward measure in general simplicial complex settings, as well as develop formal results on the information captured by the vectorization of SampEuler. While the present study focuses on 2D image masks, the pipeline extends naturally to simplicial complexes in both 2D and 3D. In particular, applying the framework to 3D images would better reflect the underlying biological structures and fur-

ther enhance the quality of the analysis pipeline introduced in this work.

Materials and Methods

MPEG-7 Dataset

The MPEG-7 shape dataset was used for benchmark shape analysis methods. We applied algorithms to fill in the holes within the objects and retained only the largest connected component inside the image. We then normalized the image sizes to be equal across all classes (See *SI Appendix* for details).

Thymus Experimental Procedure

Individual lobes from the thymi of two young wild type (C57BL/6) female mice (4 weeks of age) and five old C57BL/6 female mice (75-77 weeks of age) were collected, excess fat removed and frozen in optimal cutting temperature (OCT, TissueTek) polymer. Tissue sections were cut at $7 \mu\text{m}$ thickness and processed according to the Phenocycler-Fusion user guide (v2.1.0, Akoya Biosciences) using the Sample kit for Phenocycler-Fusion (Akoya Biosciences). Briefly, thymic tissue was fixed in acetone (Merck) for 10 minutes at room temperature, rehydrated in a hydration buffer (Akoya Biosciences) for 10 minutes and fixed in paraformaldehyde (PFA, 1.6%, Thermo Fisher Scientific) for 10 minutes at room temperature. It was then equilibrated in a staining buffer (Akoya Biosciences) for 20 minutes and stained in a staining buffer containing four blockers (Akoya Biosciences) and antibodies barcoded with DNA oligonucleotides overnight at 4°C . The tissue was washed with the staining buffer 10 minutes, fixed in 1.6% PFA for 10 minutes, washed in PBS and exposed to ice-cold methanol (Merck) for 5 minutes. After rinsing in PBS, the tissue was fixed in a fixation solution (Akoya Biosciences) for 20 minutes at room temperature, washed in PBS and stored in a storage solution (Akoya Biosciences) until loading into the Phenocycler for cyclic hybridisation with fluorescently labelled complementary oligonucleotides [55]. The barcoded antibodies listed in Table S4 were either from Akoya Biosciences or purchased from indicated providers and custom conjugated using a conjugation kit (Akoya Biosciences). Images were acquired using the Fusion slide scanner (Akoya Biosciences). The iterative imaging resulted in image stacks with 40 channels and a resolution of $0.5 \mu\text{m}/\text{pixel}$.

Thymus Image Processing and Cell Annotation

Image analysis was performed in MATLAB (R2024b). Pre-processing involved restricting the regions of interest to the individual thymus sections, thereby removing artefacts.

The background fluorescence was subtracted, and the fluorescent intensities of the markers were normalized across tissue samples. Cell segmentation was performed in two ways depending on the cell morphology. Round cell boundaries (e.g., immune cells) were outlined using Cellpose [56]. Stromal cell boundaries (e.g., TEC, fibroblasts, endothelial cells) have a more complex morphology and were therefore customly segmented using MATLAB’s `multithresh()` and `bwskel()` functions (Image Processing Toolbox), followed by pseudo-cellularization into 25x25 pixel sized tiles. For all cells and pseudo cells, centroid coordinates, area and average fluorescence intensities were exported. Cells with outlier fluorescence intensities were removed, and the fluorescence intensity of each marker was then scaled between 0 and 1. This scaling enabled the selection of marker intensity thresholds which were used to phenotype cells (see Table S5). For the positional analysis of the DN3 T cells, first the concave hulls of all samples were identified using the R(V4.5.1) package `concaveman` (V1.2.0). Next, `sf` (V1.0-22) was used to compute the shortest distance within the first 500 μm of all DN3 centroids to the capsule. Those distances were aggregated across all mice, regardless of age, and compared using base R’s implementation of the `t.test` and the `Wilcox.test`.

Euler Characteristic Transform (ECT)

ECT computations for grayscale images were performed using the `Eucalc` package (<https://github.com/HugoPasse/Eucalc>). The algorithm normalizes images to a size of 1 unit by 1 unit. We chose the range for the parameter of sublevel sets as $(-1.5, 1.5)$ to allow full inclusion of the image along all possible directions. The number of directions and sublevel set parameters were tuned for each dataset; an ablation study examining parameter sensitivity is provided in *SI Appendix*.

Ethics Statement

Both the caring for the mice and the experiments were performed in compliance with permissions of the Cantonal Veterinary Office of Basel-Stadt, Switzerland, and in accordance with Swiss federal regulations.

Data Availability

Code for generating synthetic networks, preprocessing MPEG-7 images, and computing ECT-based methods for simplicial complexes is available at <https://github.com/reddevil0623/Shape-transform-descriptor-for-thymus-structures> (DOI: <https://doi.org/10.5281/zenodo.18614535>). Thymus segmentation mask quadrants, total masks, and cell composition data for each quadrant are also available at this repository. The original MPEG-7 dataset

is publicly available from <https://dabi.temple.edu/external/shape/MPEG7/dataset.html>. Raw cell-level thymus data are available from the corresponding author upon reasonable request.

Acknowledgments

HAH, HMB, VL are grateful for the support provided by the UK Centre for Topological Data Analysis Engineering and Physical Sciences Research Council (EPSRC) grant EP/R018472/1 and EPSRC EP/Z531224/1. HAH gratefully acknowledges funding from the Royal Society RGF/EA/201074, UF150238 and EPSRC EP/Y028872/1 and EP/Z531224/1. HAH and HY acknowledge funding by the Leverhulme Trust Prize PLP-2020-252. HY is grateful for the support of the Leathersellers’ Foundation. HMB acknowledges support provided by the Mark Foundation for Cancer Research. AT and GAH are supported by the Wellcome Trust (Wellcome Collaborative Award SynThy, 211944/Z/18/Z), the Swiss National Science Foundation (310030B_138655 and 310030_215113), and the DiGeorge Syndrome Research Fund at Stanford University, generously established by an anonymous donor. LT gratefully acknowledges funding from Foundation Immune Engineering for Global Child and Adolescent Health.

Author Contributions

H.A.H., G.A.H. and H.M.B. designed research; H.Y., A.T., L.T. and V.L. performed research; H.Y., V.L., H.A.H., and H.M.B. developed new analytic tools; S.Z. performed the experiments; H.Y., A.T. and L.T. analyzed data; and H.Y., V.L., A.T., L.T., G.A.H., H.A.H., and H.M.B. wrote the paper.

Competing Interests

The authors declare no competing interests.

Supporting Information Appendix

S1 Data

We use three sources of data: synthetic network data, published MPEG-7 Core Experiment Shape-Matching dataset (MPEG-7) [57], and experimental image data of mouse thymi of different age groups. We explain the details of each dataset in turn: first the synthetic network dataset, then the preprocessing performed on the MPEG-7 dataset. Finally, we describe the thymus experiment and image processing details.

S1A Synthetic Networks

We generate a class of synthetic networks as follows. We construct each sample by first generating three edges of lengths 2, 3, and 4 with their common endpoint fixed at the origin $(0, 0)$. Each edge is discretized into $n = 100$ equally-spaced vertices (including the origin). For each edge, we select a rotation angle $\varphi \sim \text{Uniform}(0, 2\pi)$ and rotate all vertices about $(0, 0)$ by φ . For each non-origin vertex, we independently sample Gaussian noise

$$(\varepsilon_x, \varepsilon_y) \sim \mathcal{N}(0, \sigma^2), \quad \sigma = 0.02,$$

and obtain the perturbed vertex position by adding this noise to the rotated coordinates. Connectivity (line segments between consecutive edge points and from the origin to the first point of each edge) is preserved. We repeat this process $k = 20$ times to generate 20 structures for each shape class. We generate two different shape classes for comparison by choosing different angles of the three edges at the start.

S1B MPEG-7 Core Experiment Shape-Matching dataset

We use the standard MPEG-7 Core Experiment Shape-Matching (MPEG-7) dataset [57], which contains 1400 binary images of silhouettes. The images are split into 70 categories, each containing 20 images based on the same types of objects (e.g., apples, horses, etc.).

We preprocess the images by first expanding the white connected component by 1 pixel in all directions to close small gaps and filter to keep only the largest connected component. We then fill in the holes of the filtered images using [58]. To normalize across the dataset, each remaining white component is then rescaled to a fixed target area, and the image is padded with black pixels until it matches a common output size. Finally, we translate the white component so that the centroid of its white pixels coincides with the image centre. The preprocessing code is available at: <https://github.com/reddevil0623/Shape-transform-descriptor-for-thymus-structures>

S1C Thymus Experimental Procedure, Image Processing, and Cell Annotation

Individual lobes from the thymi of two young wild type (C57BL/6) female mice (4 weeks of age) and five old C57BL/6 female mice (75-77 weeks of age) were collected, excess fat removed and frozen in optimal cutting temperature (OCT, TissueTek) polymer. Tissue sections were cut at $7 \mu\text{m}$ thickness and processed according to the Phenocycler-Fusion user guide (v2.1.0, Akoya Biosciences) using the Sample kit for Phenocycler-Fusion (Akoya Biosciences). Briefly, thymic tissue was fixed in acetone (Merck) for 10 minutes at room temperature, rehydrated in a hydration buffer (Akoya Biosciences) for 10 minutes and fixed in paraformaldehyde (PFA, 1.6%, Thermo Fisher Scientific) for 10 minutes at room temperature. It was then equilibrated in a staining buffer (Akoya Biosciences) for 20 minutes and stained in a staining buffer containing four blockers (Akoya Biosciences) and antibodies barcoded with DNA oligonucleotides overnight at 4°C . The tissue was washed with the staining buffer 10 minutes, fixed in 1.6% PFA for 10 minutes, washed in PBS and exposed to ice-cold methanol (Merck) for 5 minutes. After rinsing in PBS, the tissue was fixed in a fixation solution (Akoya Biosciences) for 20 minutes at room temperature, washed in PBS and stored in a storage solution (Akoya Biosciences) until loading into the Phenocycler for cyclic hybridisation with fluorescently labelled complementary oligonucleotides [55]. The barcoded antibodies listed in Table S4 were either from Akoya Biosciences or purchased from indicated providers and custom conjugated using a conjugation kit (Akoya Biosciences). Images were acquired using the Fusion slide scanner (Akoya Biosciences). The iterative imaging resulted in image stacks with 40 channels and a resolution of $0.5 \mu\text{m}/\text{pixel}$.

Image analysis was performed in MATLAB (R2024b). Preprocessing involved restricting the regions of interest to the individual thymus sections, thereby removing artefacts. The background fluorescence was subtracted, and the fluorescent intensities of the markers were normalized across tissue samples. Cell segmentation was performed in two ways depending on the cell morphology. Round cell boundaries (e.g., immune cells) were outlined using Cellpose [56].

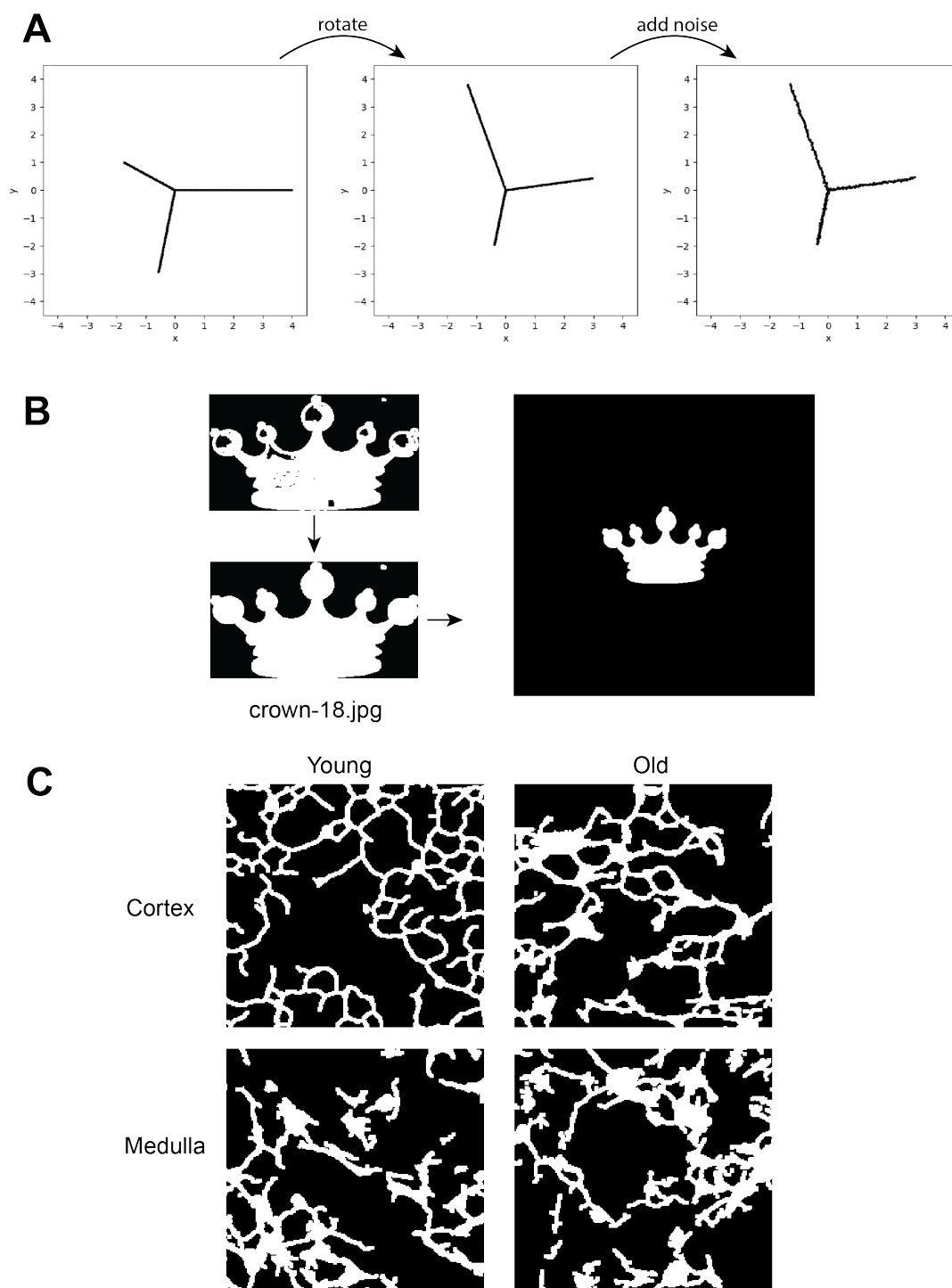


Figure S1: *A*: Pipeline for generating a class of tree samples. We first generate three edges of lengths 2, 3, and 4 from the origin, randomly oriented. We discretize each edge by sampling 100 equally spaced points along it and connecting consecutive points with edges. For each sample in the class, we randomly rotate the tree around the origin and then add coordinate-wise Gaussian noise of $\sigma = 0.02$ to each vertex. We keep the original connecting order of the edges. *B*: Preprocessing pipeline of MPEG-7 Core Experiment Shape-Matching dataset. For each image, we first expand all white connected components by 1 pixel in all directions to close small gaps and filter to keep the largest connected component. We then fill in all the holes for the filtered image using [58]. We pad black pixels around the original image to normalize all images to the same size, with the centroid of the connected component at the center of each padded image. *C*: Four example image quadrants of the mouse thymus dataset, each of size 200×200 pixels. The pixels are of side length $0.5 \mu\text{m}$. From left to right, top to bottom, they are from young-cortex, old-cortex, young-medulla, and old-medulla.

Stromal cell boundaries (e.g., TEC, fibroblasts, endothelial cells) have a more complex morphology and were therefore customly segmented using MATLAB’s `multithresh()` and `bwskel()` functions (Image Processing Toolbox), followed by pseudo-cellularization into 25x25 pixel sized tiles. For all cells and pseudo cells, centroid coordinates, area and average fluorescence intensities were exported. Cells with outlier fluorescence intensities were removed, and the fluorescence intensity of each marker was then scaled between 0 and 1. This scaling enabled the selection of marker intensity thresholds which were used to phenotype cells (see Table S5). For the positional analysis of the DN3 T cells, first the concave hulls of all samples were identified using the R(V4.5.1) package `concaveman` (V1.2.0). Next, `sf` (V1.0-22) was used to compute the shortest distance within the first 500 μm of all DN3 centroids to the capsule. Those distances were aggregated across all mice, regardless of age, and compared using base R’s implementation of the `t.test` and the `Wilcox.test`.

S2 Analysis Methods

In this section, we introduce the necessary background on topological transforms and theoretical extensions in the first section, and then in the second section, we describe other analysis methods used in this study.

S2A Topological Transforms

We recall the Euler characteristic transform (ECT) and then present a theoretical extension (Theorem S6 and Theorem S7). Next we introduce SampEuler and present desirable theoretical and practical properties of this descriptor for analysing shape datasets (Theorem S9).

The Euler Characteristic Transform

The Euler characteristic transform (ECT) is one of the foundational tools within the Topological Data Analysis community [27, 28, 19, 20].

In this section, we introduce the basic concepts of ECT for geometric simplicial complexes in order to describe our analysis methods. See [59] and [22] for a more general setting of ECT.

Definition S1. A *geometric k -simplex* K_1 is the convex hull of $k + 1$ affinely independent points v_0, v_1, \dots, v_k and denoted by $[v_0, \dots, v_k]$. For any $\{u_0, \dots, u_j\} \subset \{v_0, \dots, v_k\}$, we call $[u_0, \dots, u_j]$ a **face** of v_0, v_1, \dots, v_k . The **dimension** of K_1 is $\dim(K_1) = k$.

A *geometric simplicial complex* K is a finite collection of geometric simplices $\{K_1, \dots, K_n\}$ such that

- (i) For every $K_i \in K$, every face of K_i is also an element of K ;
- (ii) For any $K_i, K_j \in K$, either $K_i \cap K_j = \emptyset$ or $K_i \cap K_j$ is a face of both K_i and K_j .

The **dimension** of K is defined as $\max\{\dim(K_i) : i \in \{1 \dots n\}\}$.

Definition S2. For a geometric k -simplex K_1 , the Euler characteristic of K_1 , denoted by $\chi(K_1)$, is defined to be $\chi(K_1) := (-1)^k$. For a geometric simplicial complex K consisting of the finite collection $\{K_1, \dots, K_n\}$, the Euler characteristic of K is defined as $\chi(K) = \sum_{i=1}^n \chi(K_i)$.

Example 1. For any discretization K of the unit circle, there are n vertices (0-simplices) and n edges (1-simplices) forming a closed cycle for some integer n . Therefore, the Euler characteristic is $\chi(K) = n - n = 0$ for any such discretization K .

Definition S3. For geometric simplicial complex K consists of simplices K_1, \dots, K_n of dimension d , the **Euler characteristic transform** of K , denoted by $ECT(K) : S^{d-1} \times \mathbb{R} \rightarrow \mathbb{Z}$ is defined as:

$$ECT(K)(v, t) = \chi(K^{\langle v, \cdot \rangle \leq t}),$$

where $K^{\langle v, \cdot \rangle \leq t} = \{K_i : \langle v, x \rangle \leq t, \forall x \in K_i\}$. Fixing direction v , the curve $ECT(K)(v, -) : \mathbb{R} \rightarrow \mathbb{Z}$ is the **Euler characteristic curve (ECC)** of K along direction v .

We now briefly recall the notion of persistent homology and persistence diagrams; see [17, 22] for details in the context of topological transforms.

Given a topological space X , its k -th homology (with coefficients in a field) is a vector space whose dimension counts the number of independent k -dimensional “holes” of X . By 0-dimensional holes we mean connected components, by 1-dimensional holes we mean cycles or loops, and by 2-dimensional holes we mean enclosed voids. These k -dimensional holes are often called *homological features* of X .

The idea of persistent homology is to track how these homological features appear and disappear as the simplicial complex grows through a one-parameter filtration. Given a sequence of complexes $(K_t)_{t \in \mathbb{R}}$ such that $K_t \subset K_r$ for all $t \leq r$, each homological feature is born at some parameter value $a \in \mathbb{R}$ and dies at some $b > a$. The pair (a, b) records the birth and death of that feature. The multiset of all such pairs $\{(a_i, b_i)\}$ is called the *persistence diagram*. Points far from the diagonal $\{a = b\}$ correspond to long-lived, and hence typically more significant, topological features, while points close to the diagonal represent short-lived features that are often attributed to noise.

In the context of topological transforms, for a fixed direction $v \in S^{d-1}$, the height filtration $K^{\langle v, \cdot \rangle \leq t}$ gives rise to a one-parameter family of subcomplexes of K from which we can compute a persistence diagram for each homological degree.

Definition S4. For geometric simplicial complex K , the **persistent homology transform** of K denoted by $PHT(K) : S^{d-1} \rightarrow \text{Dgm}^d$ is defined as:

$$PHT(K)(v) = (PH_0(K, v), \dots, PH_{d-1}(K, v))$$

where Dgm is the space of persistence diagrams, and $PH_i(K, v)$ is the i^{th} persistent homology of K induced by the height filtration along direction v .

We use $\text{CF}(\mathbb{R})$ to denote the space of all piecewise constant functions from \mathbb{R} to \mathbb{Z} as an integer combination of half-closed and half-open intervals. The ECCs resulting from ECTs are within $\text{CF}(\mathbb{R})$.

Theorem S1 (Continuity and Hausdorffness [22]). *Given a geometric simplicial $K \subset \mathbb{R}^d$, if the ECT of K is viewed as $ECT(K) : S^{d-1} \rightarrow \text{CF}(\mathbb{R})$, a map from the space of directions to the space of ECCs, then $ECT(K)$ is Lipschitz continuous with normal metric on S^{d-1} and L_p metric on $\text{CF}(\mathbb{R})$ with $1 \leq p < \infty$. Furthermore, the space $\text{CF}(\mathbb{R})$ is a Hausdorff space.*

We fix $p = 1$ and adopt the L_1 metric for $\text{CF}(\mathbb{R})$ below, but the results hold true for any $1 \leq p < \infty$ unless stated explicitly.

Theorem S2 (Injectivity theorem [22, 23]). *Consider two geometric simplicial complexes K and L . We have $ECT(K) = ECT(L)$ if and only if $K = L$.*

The injectivity result shows that ECT can capture all geometric and topological information of the input complex. However, some differences between various complexes may not be of interest in analysis. For instance, a nonsymmetric complex K before and after applying a nontrivial rotation would generate two different ECT results.

As suggested by [60], the shape of a geometric simplicial complex K is the equivalence class of K up to rigid motions, i.e., translations, rotations, and reflections. Centring the complex K such that the sum of all vertices of K is at the origin enables rapid alignment of shapes up to translations. Throughout this paper, we assume the input complex is centred. However, no computationally cheap alignments can be performed for isometries.

Definition S5. *Given two geometric simplicial complexes K and L , we write $K \sim L$ if and only if there exists a rigid motion φ such that $\varphi(K) = L$. The relation \sim is an equivalence relation, and we define the **shape class** of K as the equivalence class $[K]$.*

We use the following definitions from [22].

Definition S6. *A geometric simplicial complex K in \mathbb{R}^d with vertex set X is **strongly generic** if:*

- (i) *ECCs are distinct for all directions $v \in S^{d-1}$,*
- (ii) *the vertex set X is in general position, i.e., no subset of k points in X lie on a $(k - 2)$ -dimension affine subspace, for $k = 2, 3, \dots, d + 1$.*

Definition S7. *For strongly generic geometric simplicial complexes $K \subset \mathbb{R}^d$, the ECT pushforward measure of K is $ECT(K)_* \mu : \mathcal{B}(\text{CF}(\mathbb{R})) \rightarrow \mathbb{R}$, such that $ECT(K)_* \mu(E) = \mu(\{v \in S^{d-1} : ECT(K)(v, -) \in E\})$, where μ is the uniform measure on the sphere and $\mathcal{B}(\text{CF}(\mathbb{R}))$ is the Borel σ -algebra on the space of ECCs.*

Theorem S3 (Theorem 6.7 of [22]). *Let K and L be strongly generic geometric simplicial complexes in \mathbb{R}^d . Let μ be the Lebesgue measure on S^{d-1} . If the pushforward measures $ECT(K)_*(\mu) = ECT(L)_*(\mu)$, then there is some $\varphi \in O(d)$ such that $L = \varphi(K)$, i.e. L and K are identical up to a combination of rotations and reflections.*

This shows that the ECT pushforward measure characterizes the shape classes of the complexes completely. Based on the ECT pushforward measure, Marsh et al. defined the Detecting Temporal shape changes with the Euler Characteristic Transform (DETECT) algorithm and applied it successfully to biological datasets [28].

Definition S8. *Given a geometric simplicial complex $K \subset \mathbb{R}^d$, and suppose that the norms of all vertices are bounded within interval $[-a, a]$. The DETECT curve of K is defined as:*

$$\begin{aligned} DETECT(K) : \mathbb{R} &\rightarrow \mathbb{R} \\ t &\rightarrow \int_{S^{d-1}} \int_{-a}^t ECT(K)(v, s) - \overline{ECT(K)(v, -)} ds dv \end{aligned}$$

where $\overline{ECT(K)(v, -)} = \int_{-a}^a ECT(K)(v, s) ds$.

Stability properties are important for data analysis. We first introduce some metrics and prove the stability property for the ECT pushforward measure in Theorem S7.

Definition S9. *Let (M, d) be a metric space and $\mathcal{P}_p(M)$ be the collection of all probability measures P such that $\int_M d(x, x_0)^p dP(x) < \infty$ for some x_0 . The p^{th} Wasserstein distance for $P, Q \in \mathcal{P}_p(M)$ is defined as:*

$$W_p(P, Q) := \left(\inf_{\gamma \in \Gamma(P, Q)} \left\{ \int_{M \times M} d(x, y)^p d\gamma(x, y) \right\} \right)^{1/p}$$

where $\Gamma(P, Q)$ is the set of all measures μ on $M \times M$ such that $\mu(A \times M) = P(A)$ and $\mu(M \times B) = Q(B)$.

Let $\Delta = \{(x, x) : x \in \mathbb{R}\}$ denote the diagonal in \mathbb{R}^2 . For a point $(b, d) \in \mathbb{R}^2$, define its projection onto the diagonal as

$$\pi_\Delta(b, d) = \left(\frac{b+d}{2}, \frac{b+d}{2} \right).$$

Definition S10 (Matching). *Given two persistence diagrams D and D' , a matching between D and D' is a map*

$$\gamma : D \cup \Delta \rightarrow D' \cup \Delta$$

where the diagonal Δ is taken with infinite multiplicity, such that:

- (i) Each point $x \in D$ is either matched to a point $\gamma(x) \in D'$, or matched to its projection $\pi_\Delta(x) \in \Delta$;
- (ii) Each point $y \in D'$ is either matched to some point in D , or matched to its projection $\pi_\Delta(y) \in \Delta$.

We denote the set of all such matchings by $\Gamma(D, D')$.

Definition S11. [61] *For $p \in [1, \infty]$, the p -Wasserstein distance between persistence diagrams D and D' is defined as*

$$W_p(D, D') = \left(\inf_{\gamma \in \Gamma(D, D')} \sum_{x \in D \cup \Delta} \|x - \gamma(x)\|_p^p \right)^{1/p},$$

where $\|\cdot\|_p$ denotes the ℓ^p -norm on \mathbb{R}^2 .

If $p = \infty$, the Wasserstein distance is defined as:

$$W_\infty(D, D') = \inf_{\gamma \in \Gamma(D, D')} \max_{x \in D \cup \Delta} \|x - \gamma(x)\|_\infty.$$

Recall the following definition taken from [22].

Definition S12. Given two geometric simplicial complexes K and L , the ECT metric between K and L is defined as:

$$d_{ECT}^1(K, L) = \int_{S^{d-1}} \|ECT(K, v) - ECT(L, v)\|_1 dv, \text{ for } 1 \leq p < \infty.$$

The ∞ -PHT distance in degree $i > 0$ between K and L is defined as:

$$d_{\infty}^{PHT^i}(K, L) = \max_{v \in S^{d-1}} W_{\infty}(Dgm_i(K, v), Dgm_i(L, v)).$$

where $Dgm_i(K, v)$ and $Dgm_i(L, v)$ are the i^{th} persistence diagrams of K and L induced by height filtration along direction v .

Theorem S4 (Proposition 2 of [62]). For geometric simplicial complex K and L in \mathbb{R}^d , we have:

$$\|ECT(K, v) - ECT(L, v)\|_1 \leq \sum_{k=0}^{d-1} 2W_{\infty}(Dgm_k(K, v), Dgm_k(L, v)),$$

where $Dgm_k(K, v)$ and $Dgm_k(L, v)$ are the k^{th} persistence diagrams of K and L induced by height filtration along direction v .

Definition S13. Let $K, L \subset \mathbb{R}^d$ be geometric simplicial complexes and let $\varphi : K \rightarrow L$ and $\psi : L \rightarrow K$ be a homotopy equivalence of M and N . Let $H_K : K \times I \rightarrow K$ and $H_L : L \times I \rightarrow L$ be homotopies from $\psi \circ \varphi$ to Id_K and from $\varphi \circ \psi$ to Id_L respectively. We denote by $\|\cdot\|_{\mathbb{R}^d}^2$ the normal Euclidean 2-norm. If there exists ϵ strictly positive such that $\|x - \varphi(x)\|_{\mathbb{R}^d}^2 \leq \epsilon$ and $\|y - \psi(y)\|_{\mathbb{R}^d}^2 \leq \epsilon$ for all $x \in K$ and $y \in L$, as well as $\|x - H_K(x, s)\|_{\mathbb{R}^d}^2 \leq 2\epsilon$ and $\|y - H_L(y, s)\|_{\mathbb{R}^d}^2 \leq 2\epsilon$ for all $x \in K, y \in L, s \in I$, then we say K and L are ϵ -controlled homotopic.

Theorem S5 (Lemma 4.5 and Theorem 4.11 of [63]). Let $K, L \subset \mathbb{R}^d$ be geometric simplicial complexes that are ϵ -controlled homotopic. Then we have:

$$\max_i d_{\infty}^{PHT^i}(K, L) \leq \epsilon.$$

Theorem S6. Let $K, L \subset \mathbb{R}^d$ be geometric simplicial complexes that are ϵ -controlled homotopic. Then we have:

$$d_{ECT}^1(K, L) \leq 2d\epsilon.$$

Proof. By the definition of the ECT metric we have:

$$\begin{aligned} d_{ECT}^1(K, L) &= \int_{S^{d-1}} \|ECT(K, v) - ECT(L, v)\|_1 dv \\ &\leq \int_{S^{d-1}} \sum_{k=0}^{d-1} 2W_{\infty}(Dgm_k(K, v), Dgm_k(L, v)) dv \\ &= \sum_{k=0}^{d-1} 2 \int_{S^{d-1}} W_{\infty}(Dgm_k(K, v), Dgm_k(L, v)) dv \\ &\leq \sum_{k=0}^{d-1} 2 \max_{v \in S^{d-1}} W_{\infty}(Dgm_k(K, v), Dgm_k(L, v)) \\ &= 2 \sum_{k=0}^{d-1} d_{\infty}^{PHT^k}(K, L) \leq 2d\epsilon. \end{aligned}$$

□

Theorem S7. The ECT pushforward measures equipped with the Wasserstein distance W_1 is Lipschitz continuous for homotopic equivalent complexes.

Proof. We know that ECT is Lipschitz continuous when equipped with d_{ECT}^1 metric from Theorem S6. It is sufficient to show that for two complexes $K, L \subset \mathbb{R}^d$, the Wasserstein distance between two pushforward measures is bounded by the ECT metric. Let $\|f - g\|_1 = \int |f(t) - g(t)| dt$ be the L_1 function metric. We have:

$$\begin{aligned} W_1(\text{ECT}(K)_*\mu, \text{ECT}(L)_*\mu) &= \inf_{\gamma \in \Gamma(\text{ECT}(K)_*\mu, \text{ECT}(L)_*\mu)} \left(\int_{\text{CF}(\mathbb{R}) \times \text{CF}(\mathbb{R})} \|f - g\|_1 d\gamma(f, g) \right) \\ &= \inf_{\gamma \in \Gamma(\text{ECT}(K)_*\mu, \text{ECT}(L)_*\mu)} \left(\int_{\text{Im}(\text{ECT}(K)) \times \text{Im}(\text{ECT}(L))} \|f - g\|_1 d\gamma(f, g) \right). \end{aligned}$$

Let $\nu_r(K, L)$ be the pushforward of the uniform measure on the sphere by the map $\text{ECT}(K, -) \times \text{ECT}(L, r(-)) : S^{d-1} \rightarrow \text{CF}(\mathbb{R}) \times \text{CF}(\mathbb{R})$. It is clear that $\nu_r(K, L) \in \Gamma(\text{ECT}(K)_*\mu, \text{ECT}(L)_*\mu)$ for all $r \in O(d)$. Then we have the following inequality:

$$\begin{aligned} W_1(\text{ECT}(K)_*\mu, \text{ECT}(L)_*\mu) &\leq \inf_{r \in O(d)} \left(\int_{\text{Im}(\text{ECT}(K)) \times \text{Im}(\text{ECT}(L))} \|f - g\|_1 d\nu_r(K, L)(f, g) \right) \\ &= \inf_{r \in O(d)} \left(\int_{S^{d-1}} \|\text{ECT}(K, v) - \text{ECT}(L, r(v))\|_1 d\mu(v) \right) \\ &\leq \inf_{r \in O(d)} d_{\text{ECT}}^1(K, r(L)). \end{aligned}$$

□

This theorem not only shows that the pushforward measure is stable under Wasserstein distance but also more stable than normal ECT outputs, as it is always less than or equal to the minimal distance between two shapes up to $O(d)$ actions.

SampEuler

The ECT pushforward measure captures all the information from shape classes of strongly generic complexes and distinguishes different shape classes. However, being a measure on a space of curves, it is hardly computable. Based on this idea, we propose the following discretization of it, called **SampEuler**, as a computable descriptor of shape classes.

Definition S14. Let $K \subset \mathbb{R}^d$ be a geometric simplicial complex and let $\text{ECT}(K)_*\mu$ be the ECT pushforward measure of K . Randomly sample $(X_1, \dots, X_n) \stackrel{\text{i.i.d.}}{\sim} \text{ECT}(K)_*\mu$. The SampEuler of K of order n , denoted SampEuler_n , is defined by

$$\text{SampEuler}_n(K) = \frac{1}{n} \sum_{i=1}^n \delta_{X_i},$$

where δ_x is the Dirac measure at x .

In practice, ECT of a given geometric simplicial complex is computed by fixing a set of evenly sampled directions around the sphere along a chosen orientation. The computation of SampEuler is simply done by randomly sampling directions from the sphere for each complex and recording the corresponding ECC curve in this random order.

For a geometric simplicial complex K , both $\text{ECT}(K)_*\mu$ and $\text{SampEuler}_n(K)$ are measures on $\text{CF}(\mathbb{R})$. We show in Theorem S8 that SampEuler_n converges to the ECT pushforward measure under the Wasserstein metrics as the order n goes to infinity. Therefore, SampEuler captures sufficient information about the shape class $[K]$ and would be more stable than normal ECT discretizations.

We will make use of the following lemma in the proof, proving in [22] along the proof of Theorem S3.

Lemma S1. For any simplicial complex K embedded in \mathbb{R}^d , the support of $\text{ECT}(K)_*\mu$ is the set $\text{Im}(\text{ECT}(K))$.

The proof of our convergence theorem is a consequence of the following classical result.

Theorem S8 (Convergence of empirical measure [64, 65]). *Suppose (M, d) is a separable metric space and $X_1, \dots, X_n \stackrel{i.i.d.}{\sim} \mu \in \mathcal{P}_r(M)$ with $r \geq 1$. Then,*

$$W_r(\mu_n, \mu) \rightarrow_{a.s.} 0 \text{ as } n \rightarrow \infty .$$

Theorem S9. *Given a geometric simplicial complex $K \subset \mathbb{R}^d$, denote $\mu_n = \text{SampEuler}_n(K)$ and $\mu_K = \text{ECT}(K)_*\mu$. Then, $W_r(\mu_n, \mu_K) \rightarrow_{a.s.} 0$ as $n \rightarrow \infty$.*

Proof. It is sufficient to check that the conditions of Theorem S8 are satisfied. We first check that $\mu_K, \mu_n \in \mathcal{P}_r(\text{CF}(\mathbb{R}))$. By the Lipschitz continuity of $\text{ECT}(K)$, there exists some constant C such that $\|\text{ECT}(K, v_1) - \text{ECT}(K, v_2)\|_1 \leq C\|v_1 - v_2\|_2 \leq 2C$. From Lemma S1, we know that the support of μ_K is the set of curves in the image of $\text{ECT}(K)$. For any $f_0 \in \text{Im}(\text{ECT}(K))$, we have

$$\int_{\text{CF}(\mathbb{R})} \|f - f_0\|_r d\mu_K(f) = \int_{\text{Im}(\text{ECT}(K))} \|f - f_0\|_r d\mu_K(f) \leq \int_{\text{Im}(\text{ECT}(K))} (2C)^r d\mu_K(f) = (2C)^r,$$

as μ_K is a probability measure. Since μ_n has finite support, it is trivial that $\mu_n \in \mathcal{P}_r(\text{CF}(\mathbb{R}))$.

Next, we show that the space of possible Euler Characteristic Curves (ECCs) is separable. We know from Theorem S1 that this space is a Hausdorff metric space using L_p metrics with $1 \leq p < \infty$. Take curves that change values at n rational numbers; this set F_n is in one-to-one correspondence with the set $(\mathbb{Q} \times \mathbb{Z})^n$, which is countable. Take the countable union $F = \cup_{i=0}^{\infty} F_n$. Since each constructible function $f \in \text{CF}(\mathbb{R})$ only has finitely many value changes, we can find $f' \in F$ arbitrarily close to f . Since F is countable, the space $\text{CF}(\mathbb{R})$ is separable. \square

Vectorization of SampEuler

As shown above, computing ECT along random directions using SampEuler has nice theoretical guarantees. However, for small biological datasets, this would lead to a high-dimensional feature, and the classification models would suffer from the curse of dimensionality. Interpreting the pushforward measure result also requires some visualization tools to help. To tackle the two problems, we propose the following vectorization algorithm, which can be used as a low-dimensional vectorization tool as well as a visualization tool of the SampEuler. It evaluates the empirical ECT pushforward measure, computed by SampEuler, on the sets of curves having constant value across certain intervals.

Definition S15. *Let K be an embedded simplicial complex in \mathbb{R}^d and $l > 0$. Denote by $\text{Int}(\mathbb{R})_l$ the set of closed intervals of length l and $K_{(a,b),c} := \{\varphi \in \text{supp}(\text{SampEuler}_n(K)) : \varphi|_{(a,b)} = c\mathbf{1}_{(a,b)}\}$ for $a, b \in \mathbb{R}$ and $c \in \mathbb{Z}$. We define the **vectorization of SampEuler** (or **vectorized SampEuler**) of K as follows:*

$$\begin{aligned} \mathcal{V}(K, l) : \text{Int}(\mathbb{R})_l \times \mathbb{Z} &\rightarrow [0, 1], \\ ([a, b], k) &\mapsto \text{SampEuler}_n(K)(K_{[a,b],k}), \end{aligned}$$

We will often abbreviate the notation to be $\mathcal{V}(K)([a, b], k)$ when l is clear from the context.

Note that the above definition is still well-defined when we use the ECT pushforward measure instead of the SampEuler of K . For theoretical purposes, we work with the definition using ECT pushforward measures. It is clear that if two complexes are equal up to isometry, they have the same ECT pushforward measure. Hence, the evaluations of this vectorization for both complexes are equal when evaluated using the ECT pushforward measure. This shows that such vectorization is isometry invariant.

Remark 1. *We can recover the average of ECT over all directions at given filtration values using the vectorization of SampEuler by:*

$$\int_{S^{d-1}} \text{ECT}(K)(v, t) dv = \int_{\mathbb{R}} \mathcal{V}(K, 0)(t, y) dy.$$

Using this observation, we can write down the explicit formula for computing DETECT [28] from the vectorization of

SampEuler:

$$\begin{aligned}
DETECT(K)(x) &= \int_{S^{d-1}} \int_{-a}^x ECT(K)(v, t) - \overline{ECT(K)(v, -)} dt dv \\
&= \int_{-a}^x \int_{S^{d-1}} ECT(K)(v, t) dv dt - \int_{-a}^x \int_{S^{d-1}} \overline{ECT(K)(v, -)} dv dt \\
&= \int_{-a}^x \int_{-\infty}^{\infty} \mathcal{V}(K, 0)(t, y) dy dt - \left(\frac{x+a}{2a}\right) \int_{S^{d-1}} \int_{-a}^a ECT(K)(v, t) dt dv \\
&= \int_{-a}^x \int_{-\infty}^{\infty} \mathcal{V}(K, 0)(t, y) dy dt - \left(\frac{x+a}{2a}\right) \int_{-a}^a \int_{-\infty}^{\infty} \mathcal{V}(K, 0)(t, y) dy dt.
\end{aligned}$$

This shows that vectorization of *SampEuler* contains all the information from *DETECT* while still being isometry invariant.

Computation Implementations

In this section, we discuss how ECT, *SampEuler*, and the vectorization of *SampEuler* are computed in applications for geometric simplicial complexes and grayscale images. We adopt Lemma S2 from [22].

Definition S16. Let K be a geometric simplicial complex. For each vertex $x \in K$, the **lower star** of X along direction v , denoted by $K^{(x,v)}$, is defined by:

$$K^{(x,v)} := \{\sigma \subset K : \max_{y \in \sigma} y \cdot v = x \cdot v\}.$$

Lemma S2. Let K be a geometric simplicial complex. Denote by $ver(K)$ the set of vertices of K . Then we have:

$$ECT(K)(v, -) = \sum_{x \in ver(K)} \chi(K^{(x,v)}) \mathbf{1}_{[x \cdot v, \infty)}.$$

Using Lemma S2, we compute the ECT of K as follows. We first fix a set of directions along a chosen orientation. For each chosen direction v , we calculate the vertex of maximum filtration value of each k -simplex $[x_0, \dots, x_k]$, i.e. we find $x_* = \operatorname{argmax}\{x_i \cdot v : i = 0, \dots, k\}$. We assign this k -simplex to the lower star of x_* . We compute the Euler characteristic of the lower star of all vertices after assigning all simplices. Without loss of generality, we assume the filtration values of all vertices are bounded in the interval $[-a, a]$. We densely sample t -values in the interval $[-a, a]$. For each t , we compute the sum $\sum_{\substack{x \in ver(K) \\ x \cdot v \leq t}} \chi(K^{(x,v)})$ as the value of $ECT(K)(v, t)$. We record all the outputs in order,

and end up with an $m \times n$ matrix representing ECT, where n is the number of directions computed and m is the number of t -values evaluated along each direction. See Figure S2 for illustration. An illustration video can be found in <https://github.com/reddevil0623/Shape-transform-descriptor-for-thymus-structures>. The computation of ECT for grayscale images is done similarly, and see [45] for more details.

The computation of *SampEuler* is similar, but with a random set of directions generated instead of the fixed set of directions. We now explain the computation of the vectorization based on the results of *SampEuler*. Without loss of generality, we assume the filtration values of all vertices along all directions are bounded within the interval $[-a, a]$ and the Euler characteristics of all possible sublevel sets are bounded within the interval $[-b, b]$. Let $\mathbb{Z}_b = \mathbb{Z} \cap [-b, b]$. We uniformly partition the space $[-a, a] \times \mathbb{Z}_b$ into constant intervals of the same length. We consider the matrix representation of *SampEuler*. For each curve represented as an array of numbers $[c_1, \dots, c_m]$, let c_i, \dots, c_j be the entries with corresponding filtration value in the interval l . If c_i, \dots, c_j are all equal to a constant c , we add 1 to the corresponding entry in the vectorization result for interval $l \times c$. Otherwise, nothing changes. We repeat the process for all curves and divide the resulting matrix by n , the number of directions, to normalize.

S2B Other Methods

Persistence Homology with Signed Distance Function

We use [66] to compute the signed distance function filtration for each thymus image by taking the boundary as the boundary contour of the white pixels. We apply [37] to compute degree 0 and degree 1 Persistence Image for each image using signed distance function filtration with a Gaussian kernel $\sigma = 1.0$ and uniform weight.

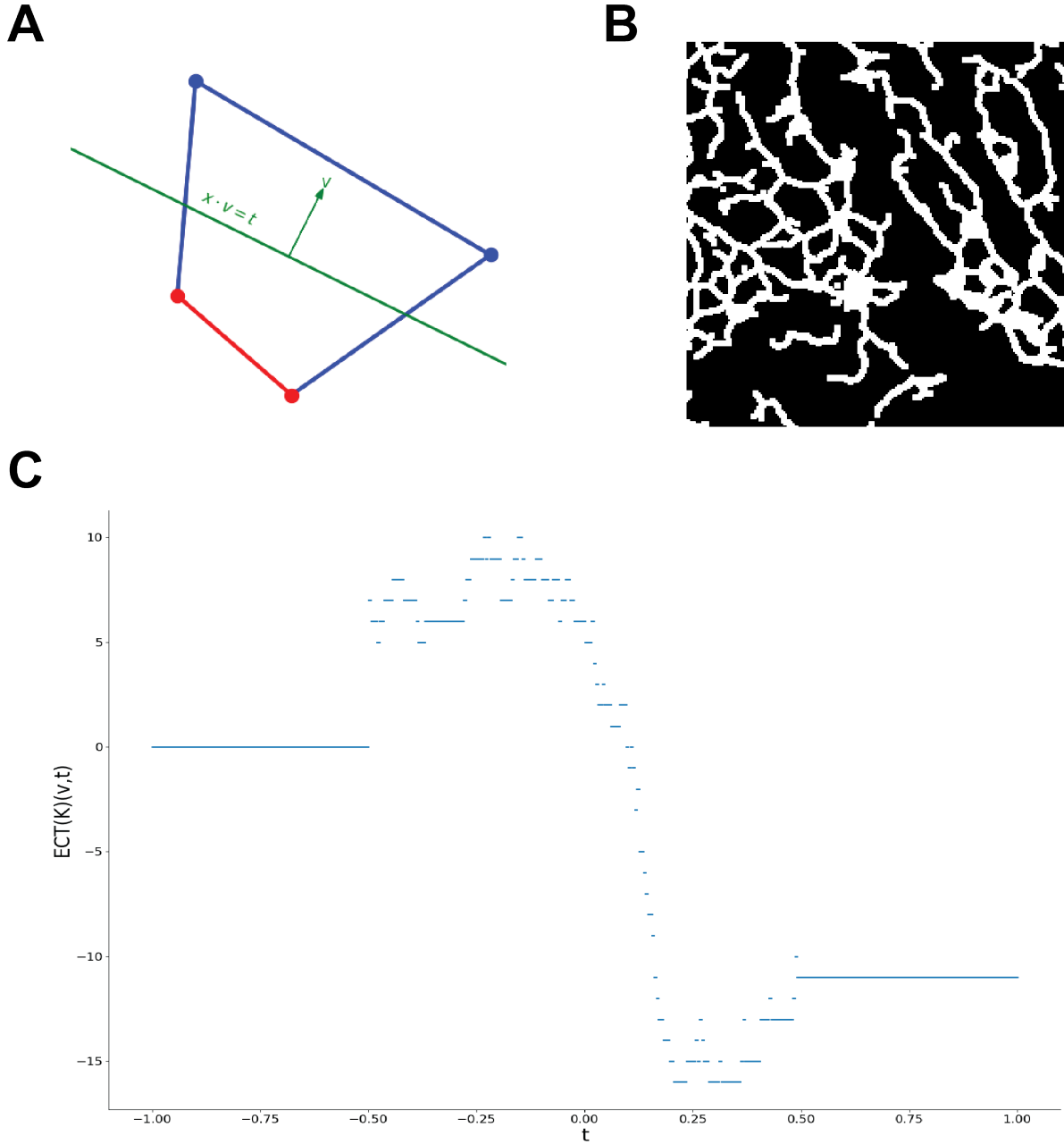


Figure S2: *A*: Schematic showing how the Euler characteristic transform (ECT) is calculated for complex K along direction v at filtration value t . The hyperplane $x \cdot v = t$ is drawn to determine the half-space $x \cdot v < t$. The vertices of K lying in this half space, together with their lower stars, are considered as plotted in red. The Euler characteristic of the red part of the shape is then computed as the output $ECT(K)(v,t)$. *B*: A segmented binary quadrant of mouse thymus. The image is of size 200 pixels \times 200 pixels. We use [45] to create a square complex of diagonal length 1 based on the image for computing ECT. *C*: Euler characteristic curve along direction $(1,0)$ for the image in *B*. The initial increase in the curve value accounts for the emergence of disjoint white pixels on the left edge of the image. As we include more of the image towards the right, white pixels connect and form loops, aligning with the fast decrease starting around filtration value -0.25 . The final increasing trend at around filtration value 0.25 is again due to the increase in connected components on the right end of the image, due to the cutting of the quadrant.

Enrichment ratio

To characterize changes in cell-type composition within each thymic region, a naive approach is to examine the raw proportion of each cell type in that region. However, with more than 40 cell types, Presel DP comprises around 60% in both age groups. This makes changes in the remaining types be obscured when using proportions alone. To better capture meaningful differences across all cell types, we instead use a cell enrichment ratio, defined as follows.

Definition S17. Consider quadrant $q \in Q$, and cell type $j \in J$. Let $C_{q,j}$ be the number of type j cells in quadrant q . Denote

$$r_{q,j} = \frac{C_{q,j} + \alpha}{\sum_{k \in J} C_{q,k} + \alpha J},$$

where α is the Dirichlet smooth constant set to avoid quadrants with few cells, and $r_{q,j}$ is the smoothed ratio of type j cell in quadrant q . Similarly, we denote

$$Y_j = \frac{(\sum_{q' \in Y} C_{q',j}) + \alpha}{(\sum_{k \in J} \sum_{q' \in Y} C_{q',j}) + \alpha J}$$

as the ratio of type j cells in all young quadrants to be used as the baseline. We define the **enrichment ratio** for quadrant q and cell type j as

$$E_{q,j} = \frac{r_{q,j}}{Y_j}.$$

We focus on cell types: DN3, Postsel DP(CD69+), Postsel DP(CD69-), Presel DP. For each quadrant q , we have a cell feature vector $(E_{q,1}, \dots, E_{q,n})$. We equip the cell feature vector space with the L_2 Euclidean norm.

S3 Data Analysis

S3A SampEuler Examples

In this section, we show how vectorization of SampEuler vectorization provides interpretable topological features. The vectorization creates an intensity map of ECC curves across all directions, revealing typical topological patterns for a given shape. We demonstrate how these patterns can be interpreted in terms of the underlying geometric structure.

We generate sets of simplicial complex representations of disjoint ellipses of major axis length 2 and minor axis length 1. We sample 80 points around the boundary of each ellipse and apply Gaussian noise with standard deviation 0.05. We create n such ellipses by randomly sampling the position of the centre and the angle of rotation. We fill all ellipses. See Figure S3.

We first show that the vectorized SampEuler can detect the connectedness of the input complex. In Figure S3A-B, the ellipse centres are uniformly distributed in a square of side length 50. Figure S3A contains 50 such ellipses, and Figure S3B contains 40 such ellipses. By definition, the final converging value of the vectorized SampEuler is equal to the total Euler characteristic of the input complex. In this case, the Euler characteristic is equal to the number of connected components. The converging value is 50 in Figure S3A and 40 in Figure S3B, indicating that Figure S3A has more connected components.

In Figure S3C-D, we show that vectorized SampEuler captures different sampling distributions used for sampling ellipse centres. The centres are restricted to quadrants 2, 3, and 4 for Figure S3C. Two general trends appear in the Euler characteristic curves. The first trend begins near filtration value -30 and rises to a peak near $+10$. This corresponds to directions pointing into quadrant 1: the growing sublevel set first encounters the ellipses at filtration values comparable to those in Figure S3A. However, the final ellipse has a lower filtration value than in Figure S3A due to the missing corner in the first quadrant, and the ellipses are more densely packed in Figure S3C, explaining the steeper trend of the curve. The second trend starts around -20 and peaks at about $+20$. This reflects curves along directions in the third quadrant: in the absence of ellipses in the first quadrant, the first ellipse is included later than in Figure S3A, shifting both the start and peak to higher filtration values. The ending filtration value matches because both Figure S3C and Figure S3A include their final ellipses, the corner ellipse in the third quadrant, at similar heights. For all other directional curves, the increasing section lies between these two extremes, yielding the ‘‘quadrilateral’’ region in the vectorized SampEuler plot.

The vectorized SampEuler in Figure S3D displays a funnel-shaped region bounded approximately by lines connecting $(-40, 0)$ to $(40, 50)$ and $(-10, 0)$ to $(10, 50)$. This pattern reflects the geometry of the elliptical sampling region. For directions near the minor axis, ellipses first appear at higher filtration values but are captured within a short interval,

producing steep ECC curves. For directions near the major axis, ellipses appear earlier but span a longer filtration range, producing shallower curves. The funnel shape emerges as ECCs transition continuously between these extremes across all sampling directions.

S3B Comparison to ECT and DETECT

In this section, we compare SampEuler and vectorized SampEuler to established topological shape descriptors. This example demonstrates that SampEuler and vectorized SampEuler capture sufficient information about the shape class of the input complex.

We use geometric simplicial complexes explained in Section S1A to illustrate that SampEuler and its vectorization are more robust to perturbations than the ECT, and are more informative than DETECT. We run two experiments for each method. In the first experiment, we generate two families of 20 complexes, with each complex randomly rotated about the origin. In the second experiment, we generate complexes without rotating them. We use mdscale [67] to visualize the results. As shown in Figure S4, ECT only distinguishes the two families of shapes correctly when all complexes are aligned. However, when we randomly rotate the complexes, the ECT fails to distinguish the two families. For DETECT, information loss during averaging means that DETECT fails to distinguish the two families in both experiments. However, with SampEuler and vectorized SampEuler, clear separation of the two classes can be seen in both experiments, showing that they are robust to isometries and contain sufficient information about the shape of input complexes.

S3C MPEG-7 Dataset for Shape Classification

To test against existing methods and understand the impact of discretization on analysis results, we apply our methods to the MPEG-7 dataset with simple normalization steps, as described in Section S1B. We first compare with methods mentioned in [33, 44]. We use the 70/30 train-test-split ratio and repeat the experiment 100 times to report the average accuracy. To be consistent with other topological pipelines, we use the Support Vector Machine (SVM) classification model [68]. We compute the pairwise Wasserstein distance for SampEuler and L_2 -distances for vectorized SampEulers and construct the RBF-kernel as input to the SVMs. Classification accuracy is reported using the best-performing parameters from the ablation study (Section S3D).

Table S1: The average accuracy (%) of different methods on the 10-class subset of the MPEG7 dataset.

Method	Accuracy
Persistence Scale Space Kernel [29]	73.33
Persistence Weighted Gaussian Kernel [30]	74.83
Sliced Wasserstein Kernel [31]	76.83
Tangent Vector Representation with Gaussian Kernel [32]	66.17
Persistence Fisher Kernel [33]	80.00
Tree Sliced Wasserstein Kernel [44]	(80.00, 85.00)*
QUPID [34]	68.80
ECT [17]	86.23
DETECT [28]	51.02
SampEuler	91.67
vectorized SampEuler	94.39

* Exact value not reported; range estimated from the bar chart in the original text.

To compare with other dedicated 2D pattern recognition methods and topological methods with deep learning, we also perform the classification task on the whole MPEG7 dataset with a 90/10 train-test-split ratio and repeat the experiments 10 times to report the average accuracy.

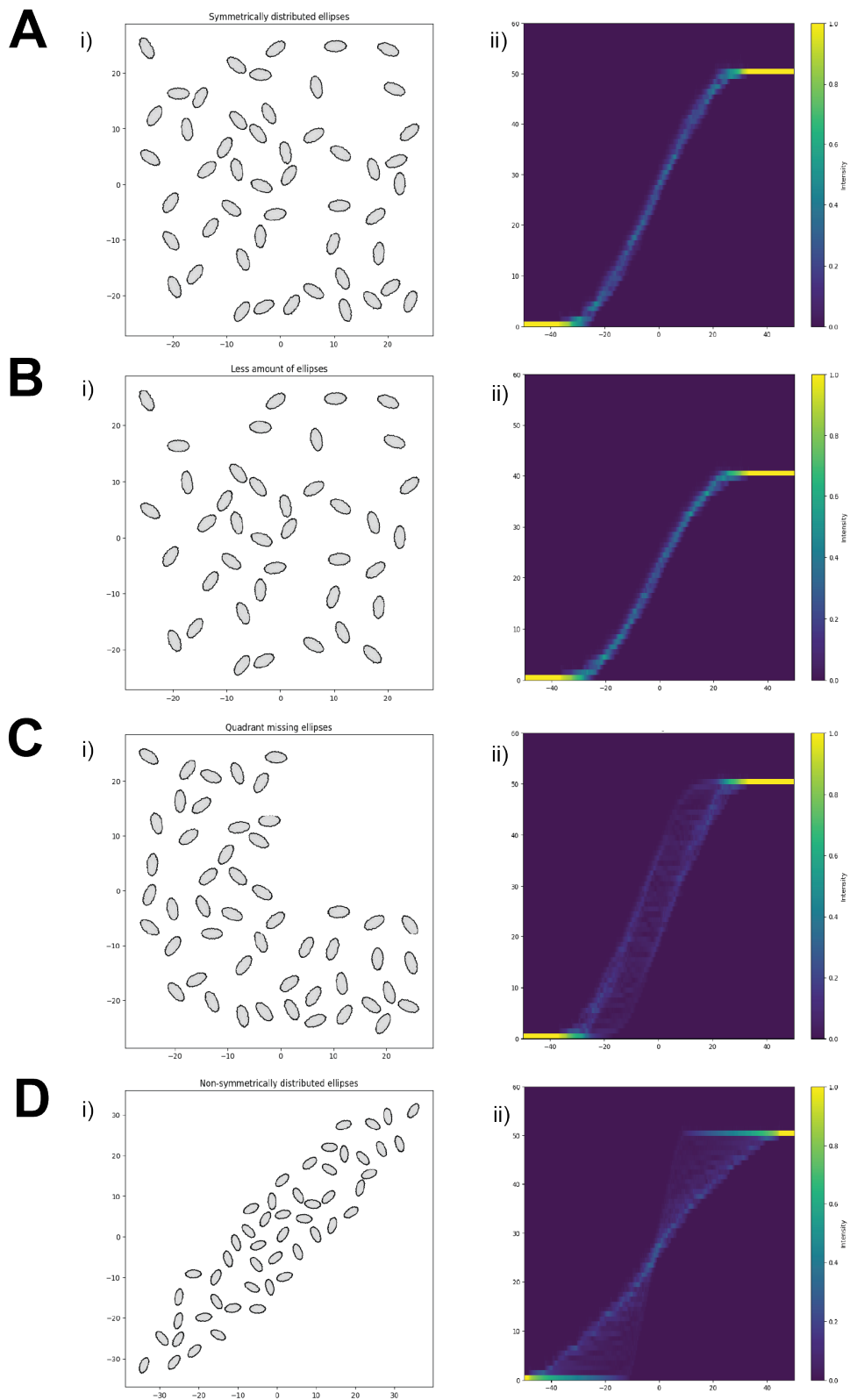


Figure S3: *A*: i) 50 geometric simplicial complex representations of ellipses with centres uniformly sampled from the centred square of side length 50. ii) The corresponding vectorized SampEuler result. *B*: i) 40 geometric simplicial complex representations of ellipses with centres uniformly sampled from the centred square of side length 50. ii) The corresponding vectorized SampEuler result. *C*: 50 geometric simplicial complex representations of ellipses with centres uniformly sampled from the restriction of quadrant 2, 3, 4 of the centred square of side length 50. ii) The corresponding vectorized SampEuler result. *D*: 50 geometric simplicial complex representations of ellipses with centres uniformly sampled from a centred ellipse with major axis length 100 and minor axis length 20. ii) The corresponding vectorized SampEuler result.

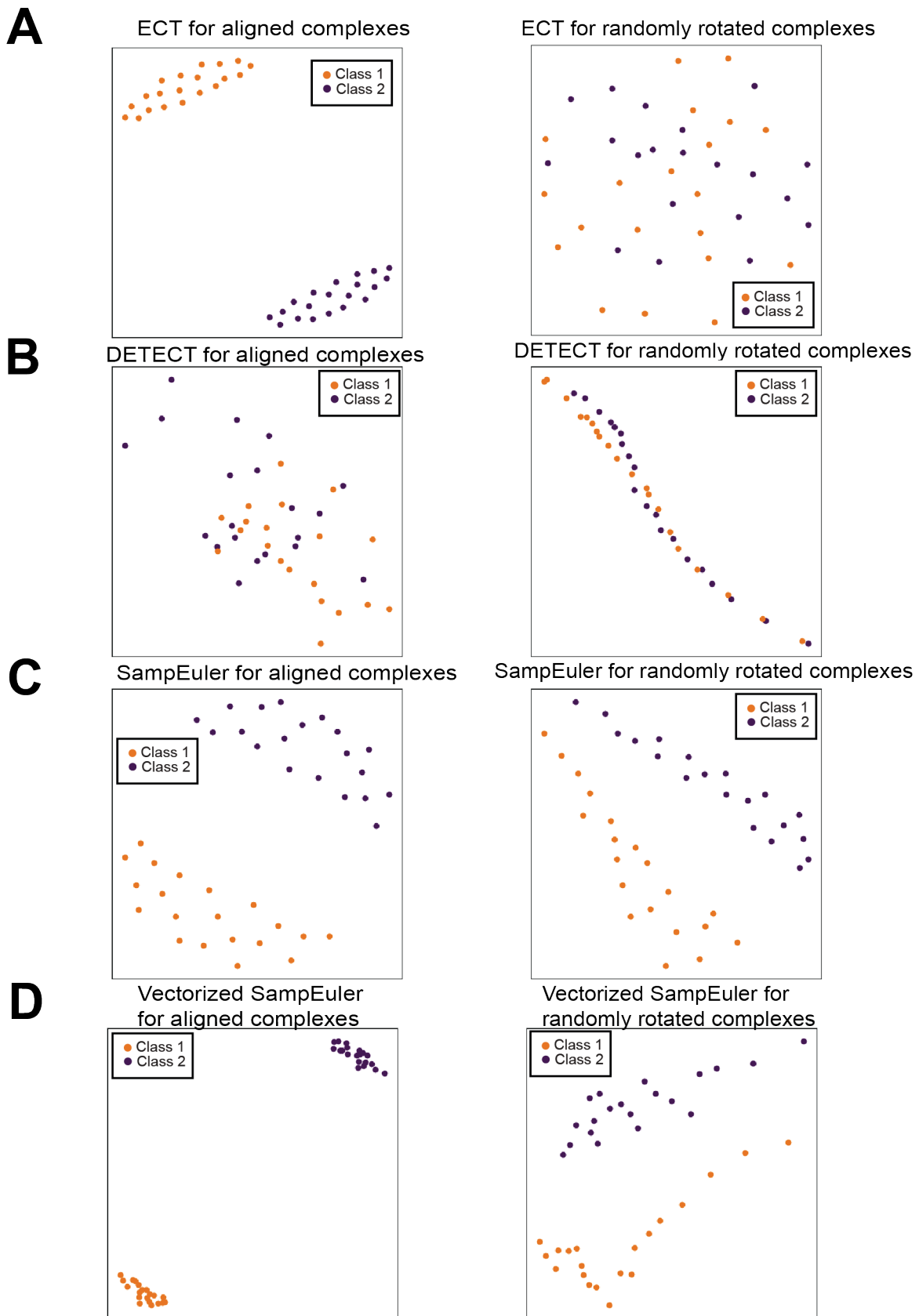


Figure S4: MDS visualizations of pairwise similarities between analysis results of two classes of generated geometric simplicial complexes. The left plots are when all complexes are aligned, and the right plots are when all complexes are randomly rotated. *A*: results of ECT. *B*: results of DETECT. *C*: results of SampEuler. *D*: results of vectorized SampEuler.

Table S2: The average accuracy (%) of different methods on the MPEG7 dataset.

Method	Accuracy
Skeleton Paths [35]	86.7
Bag of Contours [36]	97.2
Persistence Images + NN [37]	92.3
Learned Persistence Codebooks [38] + NN	92.7
ECT [17]	71.3
DETECT [28]	36.4
SampEuler	91.4
vectorized SampEuler	86.8

■ indicates our proposed methods.

As shown in Table S1, SampEuler and vectorized SampEuler provide better classification accuracies than all other methods, with vectorized SampEuler attaining the highest accuracy, likely because its vectorization step reduces feature dimensionality while maintaining all shape information. In the larger dataset of Table S2, Bag-of-Contours and neural-network-based methods attain higher accuracies than our approaches. The Bag-of-Contours method in [36] is tailored to 2D shape recognition and relies on precise boundary-contour segmentation, which can be computationally intensive and dataset-dependent. Likewise, neural networks often achieve state-of-the-art accuracy on sufficiently large training sets, though their learned representations are uninterpretable and demand substantial computational resources. Although SampEuler and vectorized SampEuler fall short of these top accuracies, they are segmentation-free, applicable to general shape analysis, and come with theoretical guarantees that support interpretability. In this larger dataset, the original SampEuler achieves better performance than its vectorized variant, presumably because its higher-resolution features can leverage the increased sample size to capture finer geometric details.

Across both datasets, SampEuler and vectorized SampEuler consistently outperform ECT- and DETECT-based baselines. DETECT suffers substantial information loss from the averaging step, leading to the worst performance overall. The high sensitivity of ECT to perturbations causes instability in classification tasks.

S3D Ablation Study

We use the MPEG7 dataset to perform the ablation study of the SampEuler method. The results are shown in Figure S5 and Figure S6. These results suggest that if we sample more than 100 directions and 1000 points along each direction, the additional information yields diminishing returns in classification accuracy. Moreover, leveraging the optimised implementation in Eucalc [45] enables efficient computation of these descriptors, making the above parameter choices practical in routine use.

S3E Quantifying Thymus Morphological Difference

We report mean classification accuracy across 50 trials and the wall-clock runtime of the ECT-based pipelines. For ECT-based methods, we compute 360 directions with 300 points along each direction. SampEulers are computed using the same parameters but with random set of directions. As a baseline, we benchmark against persistence-diagram (PD) features [37] computed from signed-distance-function (SDF) filtrations [66]. Concretely, for each binary image we compute its SDF, construct the sublevel-set filtration, and extract PDs in homology dimensions 0 and 1, thereby capturing births and deaths of connected components and loops while encoding geometry via distance to the boundary. We determine global birth and persistence ranges to set the bounding boxes, discard points with infinite death, and discretize Persistence Images (PIs) with a pixel size of $\frac{\text{global persistence range}}{500}$. PIs use a Gaussian kernel with $\sigma = 1.0$ and uniform weights; the images are then flattened into feature vectors. For both the ECT-based features and PIs, we train a random-forest classifier: we select hyperparameters via a fixed grid, refit with the best setting, and evaluate across trials.

We also compare against state-of-the-art deep learning models for image classification [46, 47, 48, 49]. For AlexNet, ViT, MobileNetV2, and EfficientNet-B0, we initialize from ImageNet-pretrained weights and replace the final layer with a two-way linear head. Inputs are resized to 224×224 RGB and normalized with ImageNet statistics. In each trial, we train using stochastic gradient descent (learning rate 10^{-3} , momentum 0.9), batch size 16, and cross-entropy loss for 5 epochs.

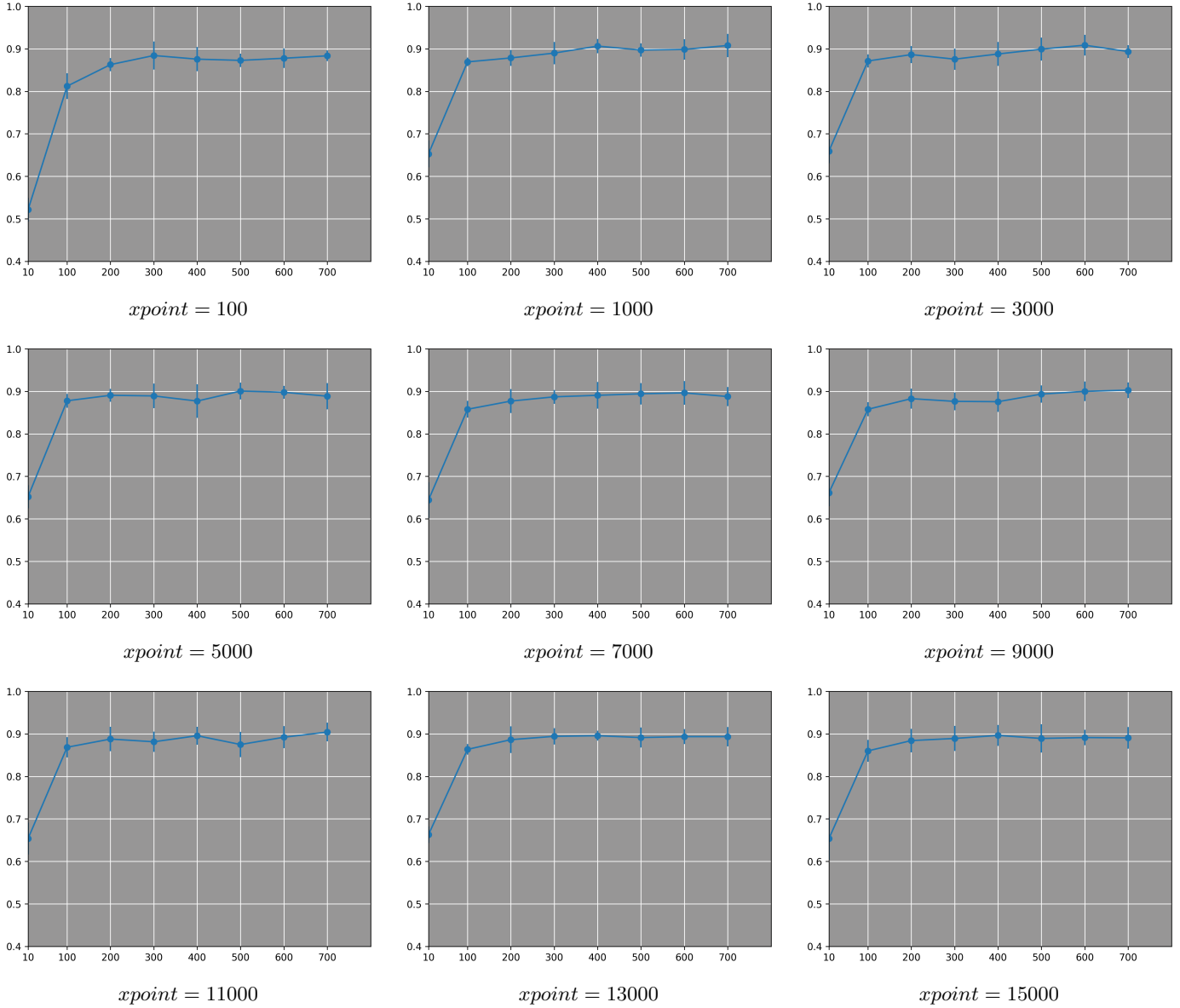


Figure S5: Ablation study of SampEuler by fixing the number of directions sampled and varying the number of filtration values along each direction.

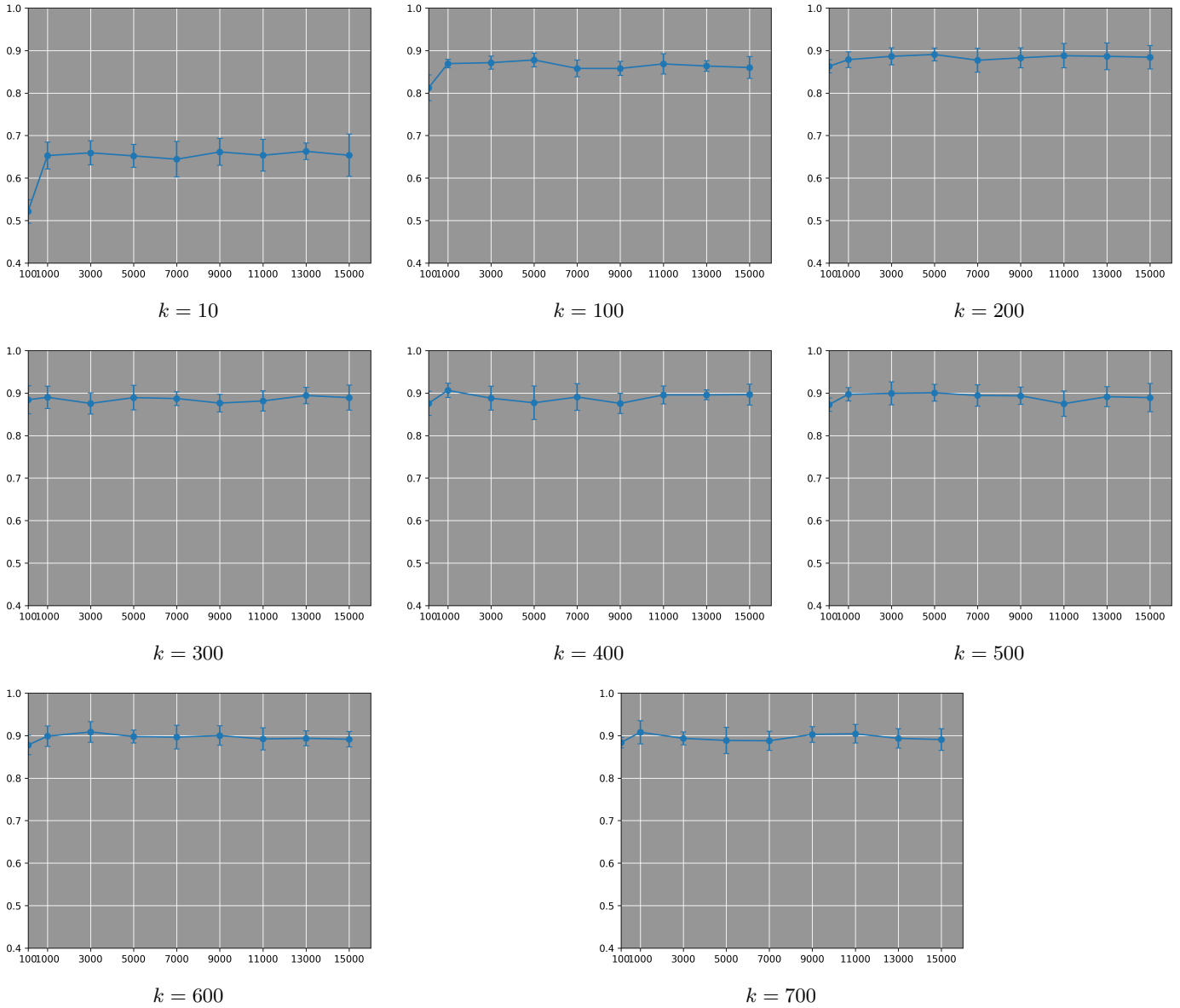


Figure S6: Ablation study of the SampEuler by fixing the number of filtration values along each direction and varying the number of directions sampled.

Table S3: The average accuracy (%) and run time of different methods on thymus K8 quadrants and K14 quadrants.

Method	K8 Acc.	K14 Acc.	K8 Time	K14 Time
PH Image [37]	0.659±0.119	0.698±0.120	2m 46.5s	3m 14.2s
AlexNet [46]	0.697±0.135	0.690±0.112	4m 18.6s	4m 17.7s
Vision Transformer [47]	0.680±0.143	0.641±0.118	32m 0.2s	31m 57.5s
MobileNet V2 [48]	0.636±0.119	0.687±0.113	24m 54.5s	24m 41.4s
EfficientNetB0 [49]	0.687±0.150	0.681±0.124	34m 23.8s	34m 15.1s
ECT	0.685±0.100	0.684±0.089	58.2s	1m 9.7s
DETECT	0.700±0.129	0.684±0.106	31.3s	29.8s
SampEuler	0.713±0.108	0.723±0.106	46.5s	42.4s
vectorized SampEuler	0.689±0.116	0.727±0.102	33.6s	28.6s

We use established methods to confirm our interpretations of the thymus structures. We compute the zeroth and first Betti numbers of images for the number of connected components and loops. The results are plotted as violin plots in Figure S7a. For K8, the violin plots for the zeroth Betti number show that young quadrants have a slightly higher number of connected components. Similarly, Betti-1 plots show that old quadrants have a higher rank for H_1 , meaning that old quadrants contain more loops. For K14, the violin plots for Betti-0 and Betti-1 both show that the old quadrants have a much larger range of variation compared with the young quadrants. These observations are consistent with our interpretations of the SHAP scores of vectorized SampEuler features.

To assess the density of holes in the cortex component, we apply the signed distance function filtration to each image so that the centres of the holes have negative distances. Now, the persistence of zeroth-degree features in persistent homology represents how dense the holes are. The further away the holes are, the longer these zeroth-degree features will persist. As shown in Figure S7b, the young quadrants have more persistent characteristics than the old quadrants. These observations are consistent with our interpretation from the gradient of vectorized SampEuler computation.

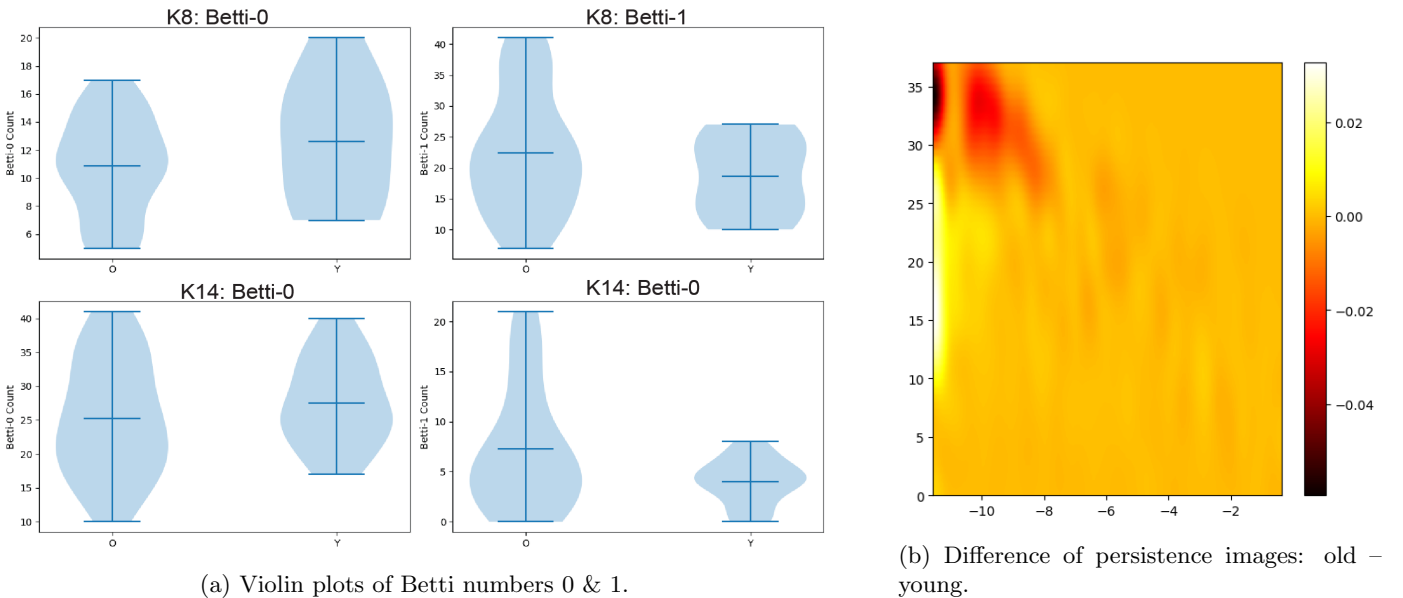


Figure S7: (a) Violin plots of Betti number 0 and Betti number 1 from top 5% to 95% of samples. (b) Difference of persistence images: $P_{old} - P_{young}$.

S3F Depth Analysis

We apply depth analysis of the cortical region to preserve the spatial heterogeneity. Since the thymus and medulla boundaries are not homotopic, we choose the following definition as the notion of depth.

Definition S18. Given a pixel p in the cortical region of the thymus, we define:

$$d_p := \min\{d(p, x), \text{ for } x \text{ in medulla}\}.$$

where d is the usual Euclidean distance. For a quadrant Q in thymus T , we define:

$$d_Q := \frac{1}{|Q|} \sum_{p \in Q} d_p.$$

We define the normalized depth of Q as follows:

$$D(Q) := 1 - \frac{d_Q}{\max_{Q' \in T} d_{Q'}}.$$

Remark 2. Since the medulla region consists of more than one connected component in all thymic samples, there is no homotopy between the thymic capsule and the cortex-medulla junction (CMJ). The above notion of depth is used when the CMJ is of interest to the study.

One could also define the distance d_p as the minimal distance to any thymic boundary point and obtain another notion of normalized depth with 0 at the capsule and 1 at the centre of the thymus. This notion of depth is more suitable when the whole thymus is of interest. We use it later for the DN cell analysis.

Based on the normalized depth of a quadrant, we construct the following depth kernel for each quadrant:

$$w_Q(t) = \exp\left(-\frac{1}{2} \left(\frac{D(Q) - t}{h}\right)^2\right).$$

We use $h = 0.1$ and normalize the weight by each age group A and get the normalized kernel $\tilde{w}_Q(t) = \frac{w_Q(t)}{\sum_{Q' \in A} w_{Q'}(t)}$. To check that the depth notion is consistent for both age groups, we plot the distribution of quadrants at various depth intervals in Figure S8. The result suggests that the shrinkage in size of the thymus due to ageing does not affect our notion of depth, and so it is suitable to compare quadrants at the same depth from different age groups to preserve the spatial heterogeneity of the cortical region.

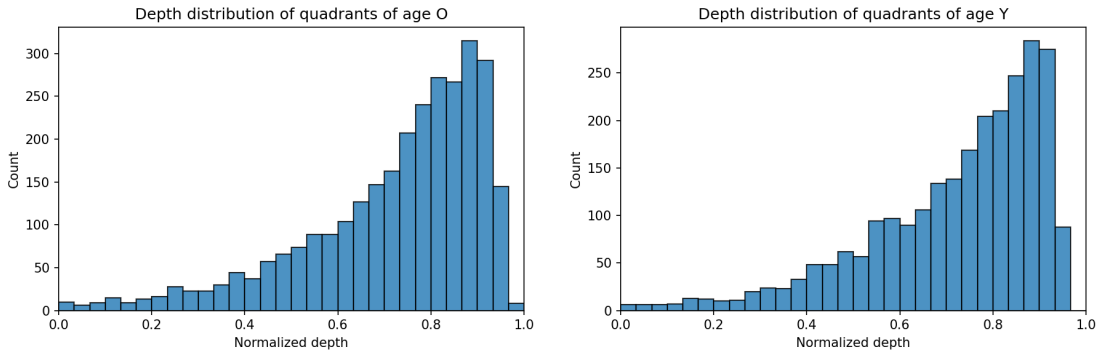


Figure S8: Depth distributions of quadrants of each age group. The x-axis is the normalized depth $D(Q)$ of each quadrant Q , and the y-axis is the count of quadrants having depth in a given depth interval.

For depth t , the normalized kernels define probability measures on quadrants for each age group,

$$P_Y^t = \sum_{Q \in Y} \tilde{w}_Q^Y(t) \delta_Q, \tag{S1}$$

$$P_O^t = \sum_{Q \in O} \tilde{w}_Q^O(t) \delta_Q, \tag{S2}$$

where δ_Q is the Dirac measure of the corresponding feature of Q . We can then compute the energy distance [50] $E(P_Y^t, P_O^t)$ between the two measures using the pairwise distance matrix M of quadrant features by

$$E(P_Y^t, P_O^t) = 2 \left(\sum_{i \in Y} \sum_{j \in O} \tilde{w}_i^Y(t) \tilde{w}_j^O(t) M_{ij} \right) - \sum_{i, j \in O} \tilde{w}_i^O(t) \tilde{w}_j^O(t) M_{ij} - \sum_{i, j \in Y} \tilde{w}_i^Y(t) \tilde{w}_j^Y(t) M_{ij}. \quad (\text{S3})$$

S3G Cell Distribution vs Morphology

For the same set of mouse thymi, we obtained cell-type and spatial locations for all cells within each thymus. Our goal is to characterize and compare age-related changes within the thymus and the epithelial architecture of the thymus. To this end, we perform k-medoids clustering [51] separately on cell-location features and on shape descriptors of thymic quadrants, and then compare the resulting cluster partitions.

To allow faster computation of the pairwise Wasserstein distance matrix while keeping sufficient information, we sample 100 directions with 3000 points along each direction, and we use the sliced Wasserstein distance algorithm [53] with 50 slices.

Since we focus on the cortical compartment, and for simplicity, we restrict the compositional analysis of haematopoietic cells to **DN3**, **Presel DP**, **Postsel DP (CD69+)** and **Postsel DP (CD69-)** thymocytes. These cell types not only constitute the vast majority of cortical thymocytes but are also centered around the developmentally-relevant process of positive selection.

We discuss how to choose the number of clusters for both clusterings. We first applied silhouette analysis [51] to find the most suitable number of clusters from the set $\{2, 3, \dots, 10\}$ for both k-medoids clusterings. The analysis suggests $k = 2$ for both the clustering based on enrichment ratios and the clustering based on SampEulers. The results are shown in Figure S9 and Figure S10. Two clusters are not able to provide meaningful biological interpretations about the impact of the ageing process. Therefore, we manually force three clusters for both clusterings as the second-highest silhouette score choice. To further constrain the analysis to look at cells in direct contact with thymic epithelial cells (TECs), we filter to only count cells of selected cell types that are at a distance less than or equal to $5 \mu\text{m}$ from a TEC. The results are shown in Figure S11 and Figure S12.

Table S4: PhenoCycler antibody panel with host species, clone, vendor, catalogue number, fluorophore, dilution, and exposure time. DAPI was imaged at every round. For the other markers, the order in which they appear in the table represents the order in which they were imaged in groups of three (see Materials and Methods). Ar Hms = Armenian hamster, Ms = mouse, Rb = rabbit, Rt = rat, Sy Hms = Syrian hamster

Marker	Host species	Clone	Vendor	Catalogue number	Fluorophore	Dilution	Exposure time [ms]
DAPI	-	-	-	-	-	1:1000	150
AIRE	Rt	5H12	Invitrogen	14-5934-82	Cy5	1:200	200
B220	Rt	Ra3-6B2	Akoya	4150006	AF488	1:200	200
CD8A	Rt	53-6.7	Akoya	4250017	ATTO550	1:200	150
FOXP3	Rt	FJK-16s	Invitrogen	14-5773-82	Cy5	1:200	200
TCRGD	Ar Hms	GL3	BioLegend	118128	AF488	1:100	300
NP63	Rb	polyclonal	Proteintech	12143-1-AP	ATTO550	1:200	300
PD1	Rt	29F.1A12	Invitrogen	P378-1MG	Cy5	1:200	300
CD86	Rt	GL-1	Invitrogen	MA1-10299	AF488	1:200	300
CD69	Ar Hms	H1.2F3	Invitrogen	14-0691-82	ATTO550	1:200	300
CD11C	Ar Hms	N418	Akoya	4350013	Cy5	1:200	300
CD45	Rt	30-F11	Akoya	4150002	AF488	1:200	150
ICOS	Ar Hms	C398.4A	Invitrogen	14-9949-82	ATTO550	1:200	200
XCR1	Ms	ZET	BioLegend	148202	Cy5	1:100	300
PDCA1	Rt	eBio927	Invitrogen	16-3172-81	AF488	1:200	300

Continued on next page

Table S4 – continued from previous page

Marker	Host species	Clone	Vendor	Catalogue number	Fluorophore	Dilution	Exposure time [ms]
SIRPA	Rt	P84	Invitrogen	16-1721-81	ATTO550	1:100	300
LY6G	Rt	1A8	Akoya	4350015	Cy5	1:200	100
CD71	Rt	R17217	Invitrogen	17-0711-82	AF488	1:200	300
KI67	Ms	B56	Akoya	4250019	ATTO550	1:200	150
SCA1	Rt	D7	Invitrogen	14-5981-85	Cy5	1:200	200
CD25	Rt	PC61.5	Invitrogen	14-0251-86	AF488	1:200	300
HELIOS	Ar Hms	22F6	BioLegend	137202	ATTO550	1:200	200
K10	Rb	polyclonal	Invitrogen	PA5-104456	Cy5	1:400	80
CD62L	Rt	95218	R&D	MAB5761	AF488	1:200	200
CD5	Rt	53-7.3	Akoya	4250007	ATTO550	1:200	250
ERTR7	Rt	ER-TR7	Bio-Rad	MCA2402	Cy5	1:400	80
CD24	Rt	M1/69	Akoya	4150014	AF488	1:200	200
CD31	Rt	MEC13.3	Akoya	4250001	ATTO550	1:200	200
CD49F	Rt	GoH3	Akoya	4350007	Cy5	1:200	200
CD11B	Rt	M1/70	Akoya	4150015	AF488	1:200	200
CD4	Rt	RM4-5	Akoya	4250016	ATTO550	1:200	150
LY51	Rt	6C3	BioLegend	108302	Cy5	1:100	300
PIGR	Rb	polyclonal	Invitrogen	PA5-35340	AF488	1:200	250
MHCII	Rt	M5/114.15.2	Akoya	4250003	ATTO550	1:400	150
TCRB	Ar Hms	H57-597	Akoya	4350006	Cy5	1:200	150
PDPN	Sy Hms	8.1.1	Invitrogen	MA5-18054	AF488	1:200	300
CD206	Rt	C068C2	BioLegend	141701	ATTO550	1:400	250
K8	Rt	TROMA-1	EMD Millipore	MABT329	Cy5	1:200	80
K14	Rb	polyclonal	Invitrogen	PA5-16722	AF488	1:200	80
CD44	Rt	IM7	Akoya	4250002	ATTO550	1:200	200

Table S5: List of PhenoCycler cell phenotypes with their defining marker thresholds, distance thresholds, and regional filters.

No.	Phenotype name	Corresponding cell type	Defining markers and their normalized expression thresholds	Distance thresholds [pixels]	Region filter
1	ICOS+	T-cells expressing ICOS	ICOS > 0.25	7	-
2	T-reg	Regulatory T-cells	FOXP3 > 0.15	6	-
3	CD11b+	Monocytes	CD11b > 0.15	8	-
4	T-gd (PD1+)	gd T-cells expressing PD1	(TCRgd > 0.15) & (PD1 > 0.25)	6	-
5	T-gd (PD1-)	gd T-cells not expressing PD1	(TCRgd > 0.15) & (PD1 ≤ 0.25)	6	-
6	DN3	DN T-cells	(CD44 ≤ 0.2) & (CD25 > 0.2) & (CD5 ≤ 0.2) & (TCRb ≤ 0.2)	6	Cortex
7	ISP8	Immature SP8 T-cells	(CD25 ≤ 0.2) & (CD8a > 0.3) & (CD4 ≤ 0.2) & (CD5 ≤ 0.2) & (TCRb ≤ 0.2)	-	Cortex

Continued on next page

Table S5 – continued from previous page

No.	Phenotype	Cell type	Markers and Expression Thresholds	Dist. [px]	Region
8	SP8 (CD69+)	SP8 T-cells expressing CD69	(CD8a > 0.3) & (CD4 ≤ 0.2) & ((TCRb > 0.15) (CD5 > 0.15)) & (CD69 > 0.25)	-	Medulla
9	SP8 (CD69-)	SP8 T-cells not expressing CD69	(CD8a > 0.3) & (CD4 ≤ 0.2) & ((TCRb > 0.15) (CD5 > 0.15)) & (CD69 ≤ 0.25)	-	Medulla
10	MP	Macrophages	CD206 > 0.075	8	-
11	BC	B cells	B220 > 0.1	4 for BC clusters, 6 for interspersed BC	-
12	SP4 (Helios+)	SP4 T-cells expressing Helios	(CD8a ≤ 0.2) & (CD4 > 0.2) & ((TCRb > 0.15) (CD5 > 0.15)) & (Helios > 0.15)	-	Medulla
13	pDC (PDCA1+)	Plasmacytoid dendritic cells expressing PDCA1	(CD11c > 0.25) & (PDCA1 > 0.25)	11	-
14	cDC1 (XCR1+)	Conventional dendritic cells expressing XCR1	(CD11c > 0.25) & (XCR1 > 0.35)	11	-
15	cDC2 (SIRPa+)	Conventional dendritic cells expressing SIRPa	(CD11c > 0.25) & (PDCA1 > 0.25)	11	-
16	DC (CD11c+)	Remaining dendritic cells expressing CD11c	CD11c > 0.25	11	-
17	SP4 (CD69+)	SP4 T-cells expressing CD69	(CD8a ≤ 0.2) & (CD4 > 0.2) & ((TCRb > 0.2) (CD5 > 0.15)) & (CD69 > 0.25)	-	Medulla
18	SP4 (CD69-)	SP4 T-cells not expressing CD69	(CD8a ≤ 0.2) & (CD4 > 0.2) & ((TCRb > 0.2) (CD5 > 0.15)) & (CD69 ≤ 0.25)	-	Medulla
19	Postselection DP (CD69+)	DP T-cells that have undergone selection and express CD69	(CD4 > 0.2) & (CD8a > 0.2) & ((CD5 > 0.3) (TCRb > 0.2)) & (CD69 > 0.25)	-	Cortex
20	Postselection DP (CD69-)	DP T-cells that have undergone selection and do not express CD69	(CD4 > 0.2) & (CD8a > 0.2) & ((CD5 > 0.3) (TCRb > 0.3)) & (CD69 ≤ 0.25)	-	Cortex
21	Preselection DP	DP T-cells that have not undergone selection	(CD4 > 0.05) & (CD8a > 0.05) & ((CD5 ≤ 0.3) (TCRb ≤ 0.3)) & (CD69 ≤ 0.3)	-	Cortex
22	mTEC (Aire+)	mTEC expressing Aire	Aire > 0.09	9	-
23	mTEC (Ly6g+)	mTEC expressing Ly6g	Ly6g > 0.09	14	-
24	mTEC (PIGR+)	mTEC expressing PIGR	PIGR > 0.18	11	Medulla
25	mTEC (K10+)	mTEC expressing K10	K10 > 0.1	-	-
26	mTEC (CD49f+)	mTEC expressing CD49f	(K14 > 0.1 K8 > 0.1) & (CD49f > 0.3) & (PDPN < 0.15)	-	Medulla
27	mTEC hi (K14+, CD86+)	mTEC expressing K14, CD86, and MHCII	(K14 > 0.1) & (MHCII > 0.35) & (CD86 > 0.2)	-	-

Continued on next page

Table S5 – continued from previous page

No.	Phenotype	Cell type	Markers and Expression Thresholds	Dist. [px]	Region
28	mTEC hi (K8+, CD86+)	mTEC expressing K8, CD86, and MHCII	(K8 > 0.1) & (MHCII > 0.35) & (CD86 > 0.2)	-	Medulla
29	TEC (PDPN+)	TEC expressing PDPN	(K14 > 0.1 K8 > 0.1 Np63 > 0.1) & (PDPN > 0.15) & (ERTR7 < 0.15)	5	-
30	mTEC hi (K14+, CD86-)	mTEC expressing K14, MHCII, but not CD86	(K14 > 0.1) & (MHCII > 0.35) & (CD86 ≤ 0.2)	-	-
31	mTEC hi (K8+, CD86-)	mTEC expressing K8, MHCII, but not CD86	(K8 > 0.1) & (MHCII > 0.35) & (CD86 ≤ 0.2)	-	Medulla
32	mTEC lo (K14+)	mTEC expressing K14 but not MHCII	(K14 > 0.1) & (MHCII ≤ 0.35)	-	-
33	mTEC lo (K8+)	mTEC expressing K8 but not MHCII	(K8 > 0.1) & (MHCII ≤ 0.35)	-	Medulla
34	cTEC hi (Ly51+)	cTEC expressing Ly51 and MHCII	(K8 > 0.1) & (MHCII > 0.35) & (Ly51 > 0.2)	-	Cortex
35	cTEC lo (Ly51+)	cTEC expressing Ly51 but not MHCII	(K8 > 0.1) & (MHCII ≤ 0.35) & (Ly51 > 0.2)	-	Cortex
36	cTEC hi (Ly51-)	cTEC expressing MHCII but not Ly51	(K8 > 0.1) & (MHCII > 0.35) & (Ly51 ≤ 0.2)	-	Cortex
37	cTEC lo (Ly51-)	cTEC expressing neither Ly51 nor MHCII	(K8 > 0.1) & (MHCII ≤ 0.35) & (Ly51 ≤ 0.2)	-	Cortex
38	Endo	Endothelial cells	CD31 > 0.2	-	-
39	Fb (PDPN+, ERTR7-)	Fibroblasts expressing PDPN but not ERTR7	(PDPN ≥ 0.15) & (ERTR7 < 0.15) & (Np63 < 0.1)	-	-
40	Fb (PDPN-, ERTR7+)	Fibroblasts expressing ERTR7 but not PDPN	(PDPN < 0.15) & (ERTR7 ≥ 0.15) & (Np63 < 0.1)	-	-
41	Fb (PDPN+, ERTR7+)	Fibroblasts expressing both PDPN and ERTR7	(PDPN ≥ 0.15) & (ERTR7 ≥ 0.15) & (Np63 < 0.1)	-	-

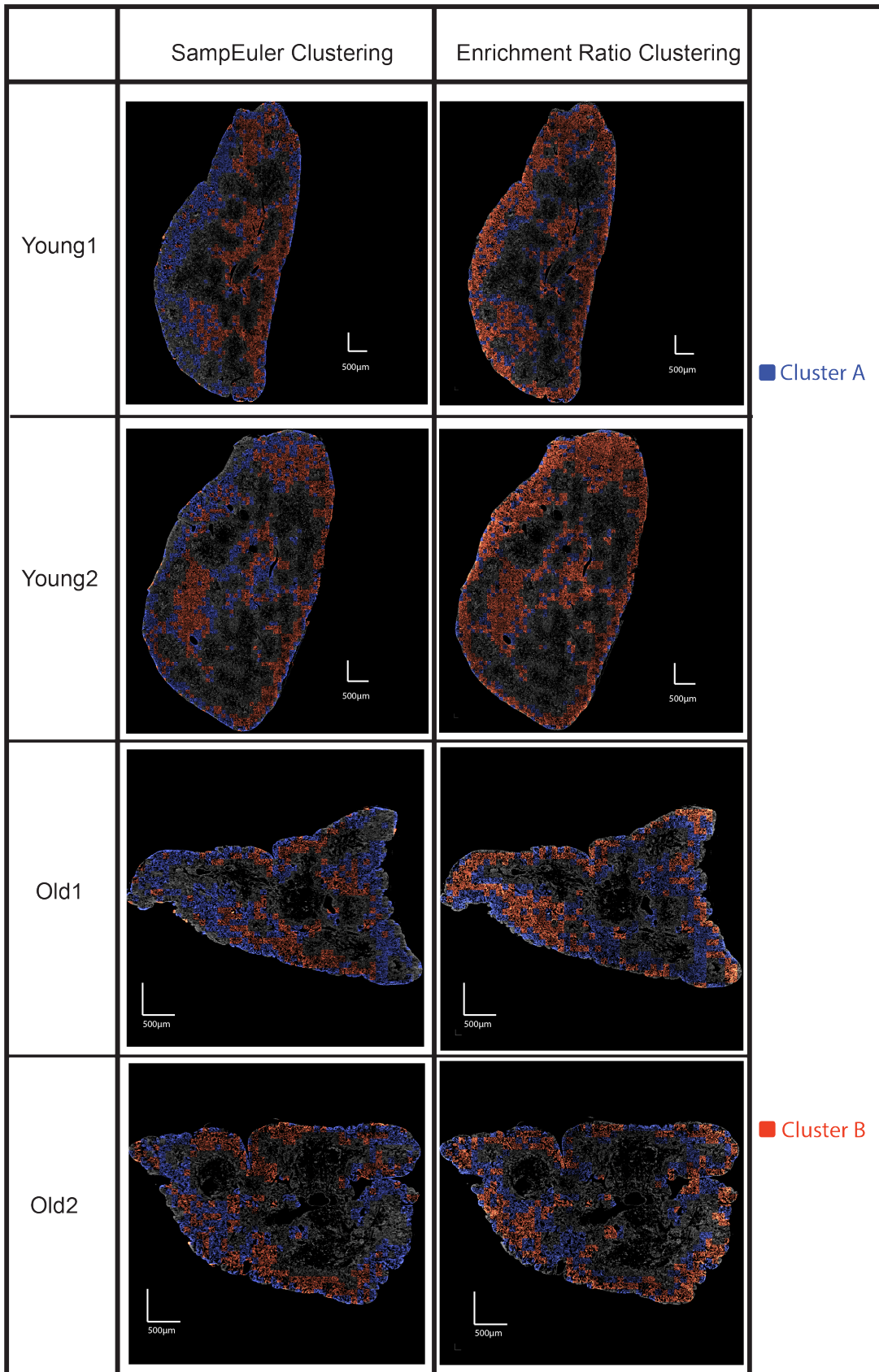


Figure S9: K-medoids clustering results with 2 clusters for all thymic cortex quadrants. This plot contains result for the first four thymi, the remaining results are included in Figure S10. The first column on the left is the results using SampEulers, the second column is the results using cell enrichment ratios.

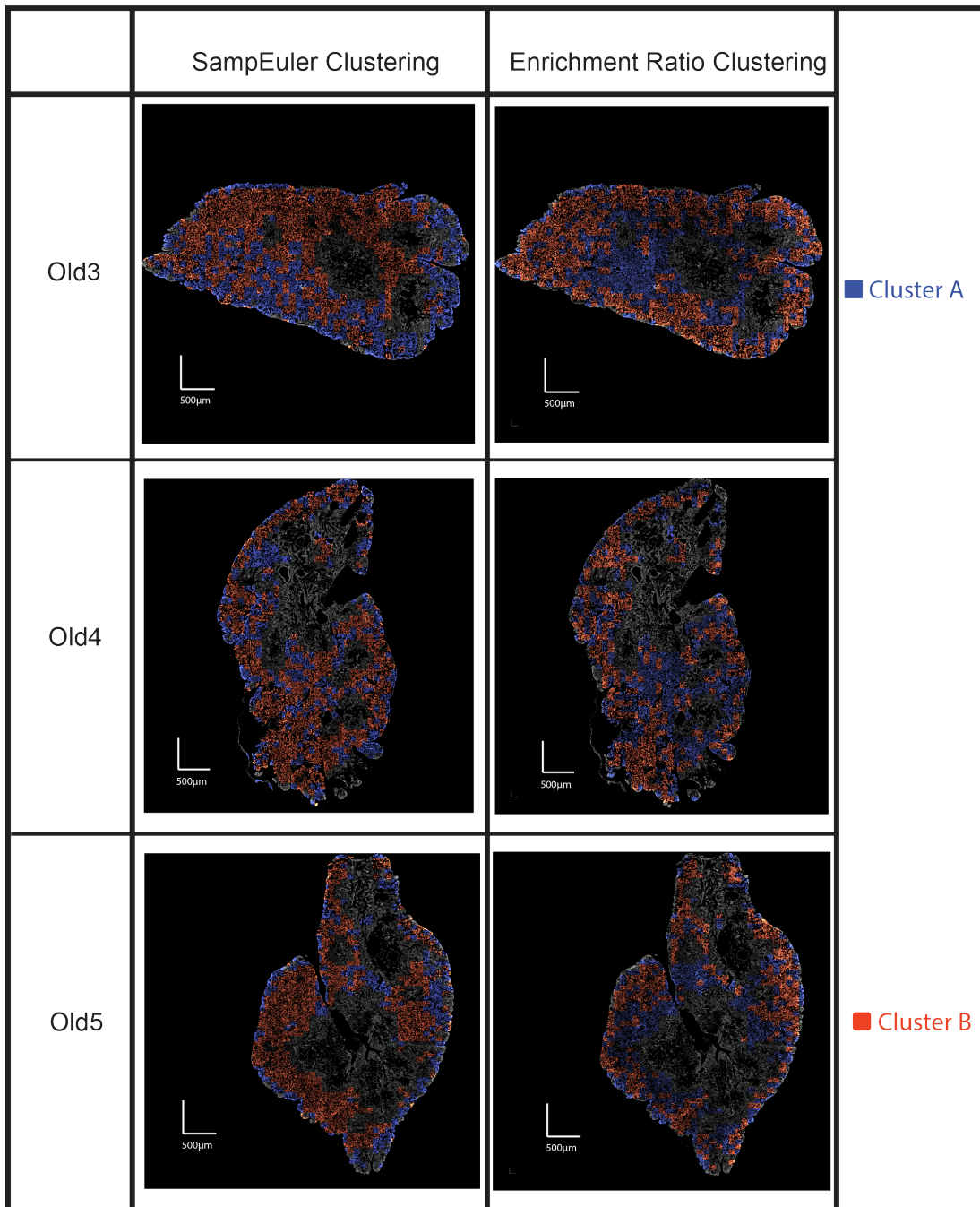


Figure S10: K-medoids clustering results with 2 clusters for all thymic cortex quadrants. This plot contains result for the remaining thymi continuing from Figure S9. The first column on the left is the results using SampEulers, the second column is the results using cell enrichment ratios.

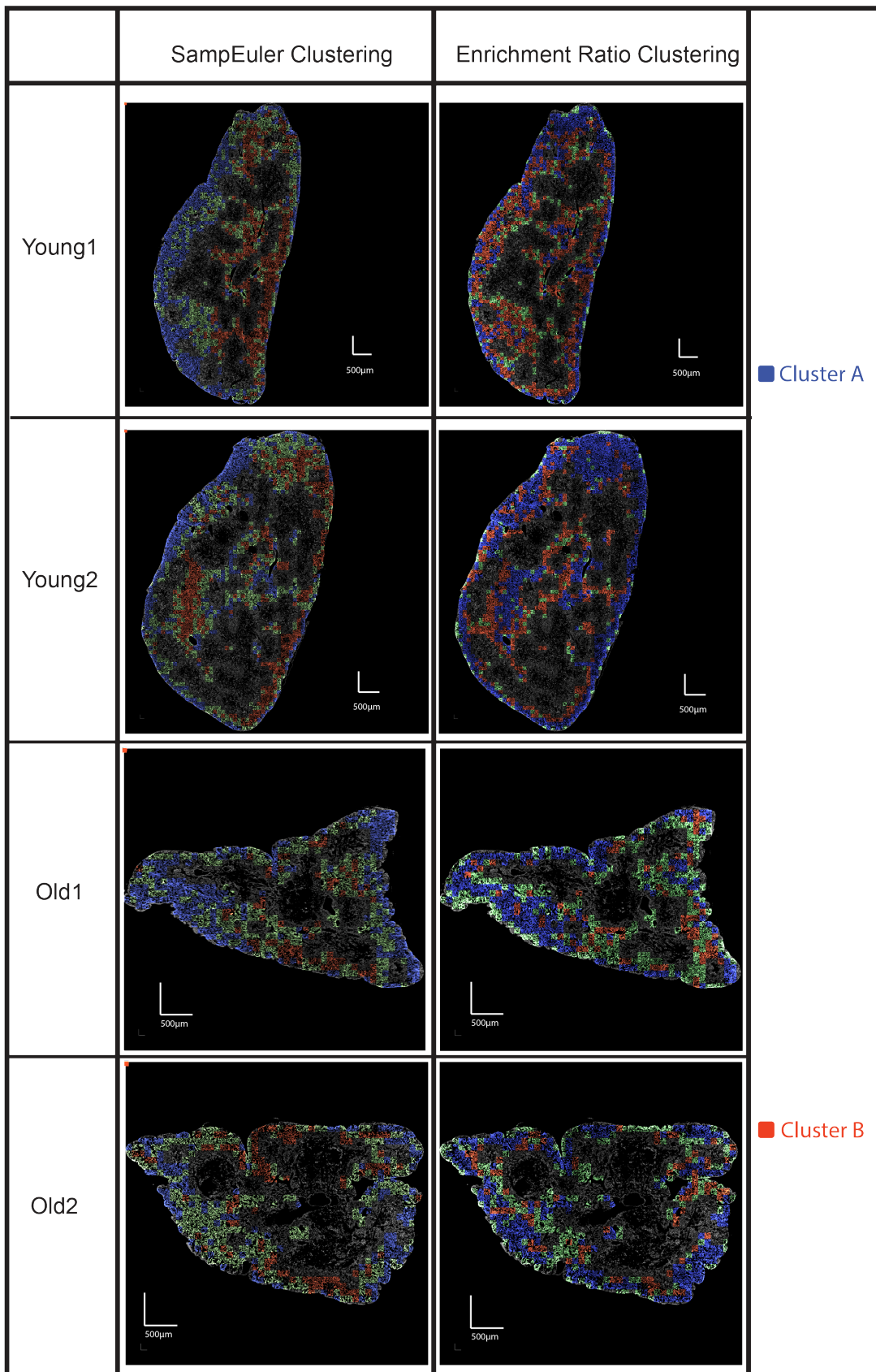


Figure S11: K-medoids clustering results for all thymic cortex quadrants using 3 clusters. This plot contains results for the first four thymi, the remaining results are included in Figure S12. The first column on the left is the results using SampEulers, the second column is the results using selected cell enrichment ratios.

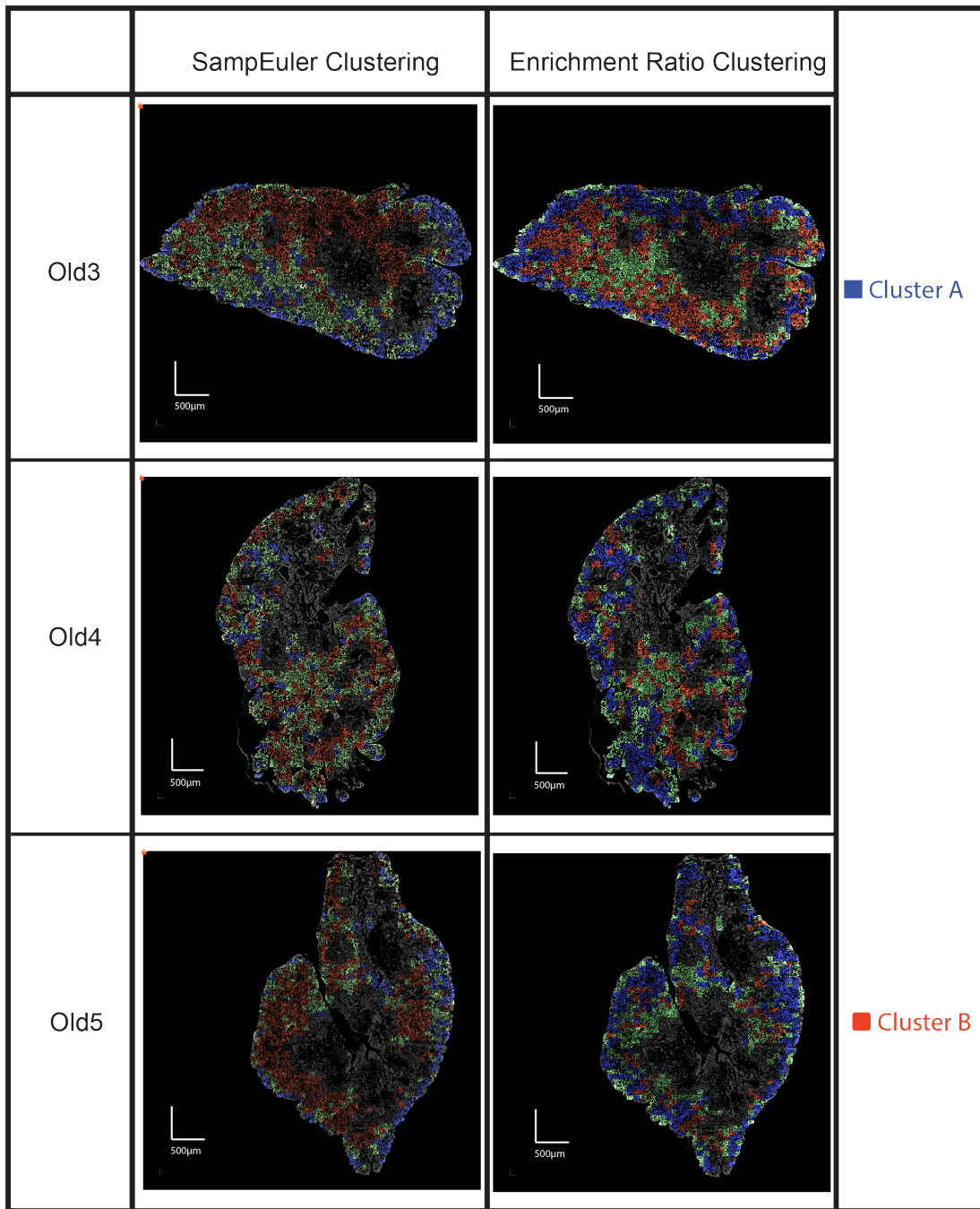


Figure S12: K-medoids clustering results for all thymic cortex quadrants using 3 clusters. This plot contains results for the remaining thymi continuing from Figure S11. The first column on the left is the results using SampEulers, the second column is the results using cell enrichment ratios.

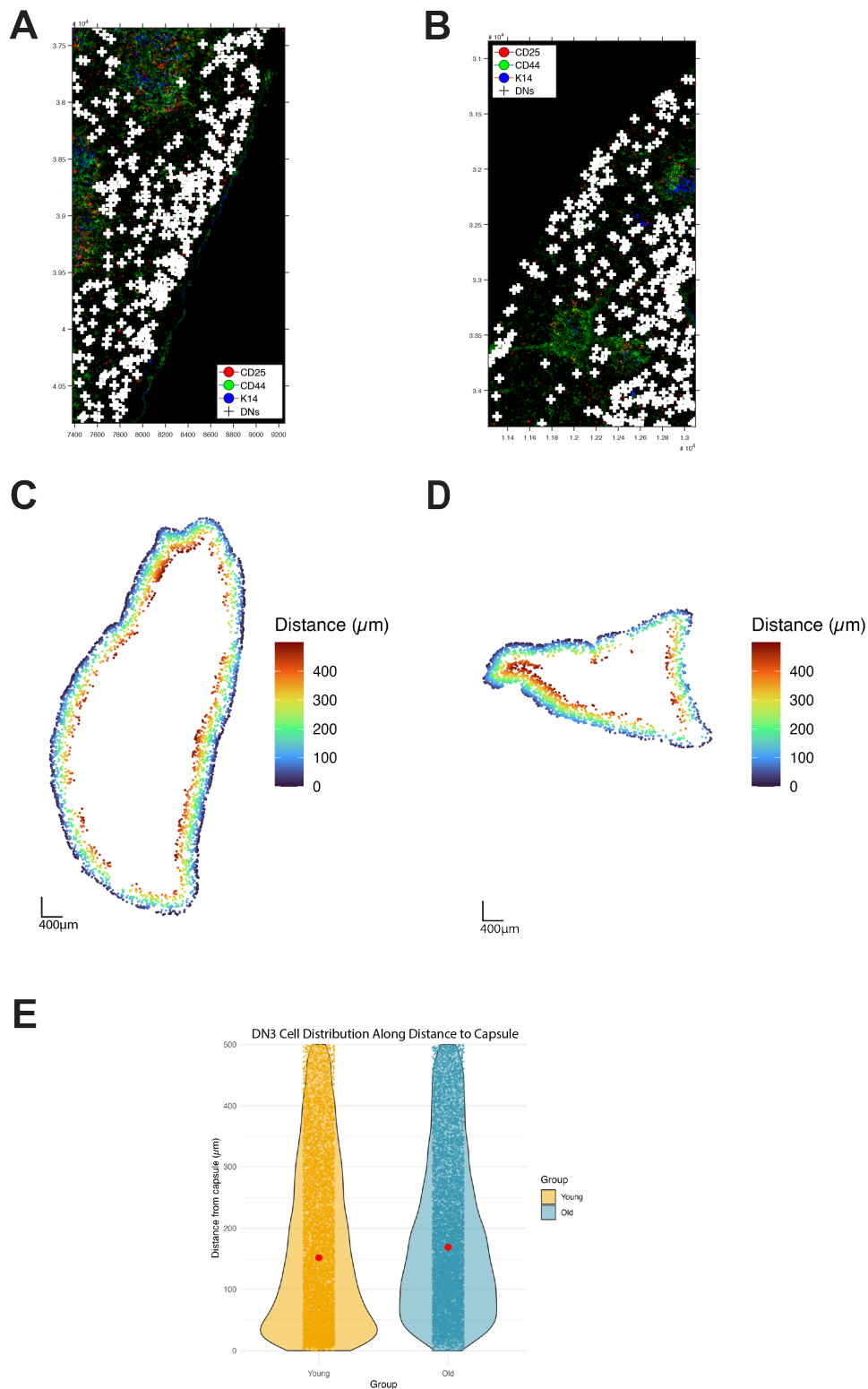


Figure S13: Qualitative assessment of DN3 localization characterized by CD4⁻, CD8a⁻, CD5⁻, CD44⁻, CD25⁺, CD45⁺ for a young *A* and an old thymus tissue *B*. A close-up of the sub-capsular/deep-cortical area is represented for each age. One x,y-unit corresponds to 0.5 μm . *C* and *D* Spatial scatter plots illustrating the spatial location of DN3s within a set distance of 500 μm from the capsule for a young and an old thymus, respectively. *E* Violin plot of individual DN3 distances from the capsule split by age group. The quantification is based on the whole dataset (2 young and 5 old samples). These distributions were compared using a two-sample t-test ($p = 6.3\text{e-}11$) and a Wilcox test ($p = 3.1\text{e-}18$).

References

- [1] Johannes Betge, Niklas Rindtorff, Jan Sauer, Benedikt Rauscher, Clara Dingert, Haristi Gaitantzi, Frank Herweck, Kauthar Srour-Mhanna, Thilo Miersch, Erica Valentini, et al. The drug-induced phenotypic landscape of colorectal cancer organoids. *Nature Communications*, 13(1):3135, 2022.
- [2] Rita Rezzani, Lorenzo Nardo, Gaia Favero, Michele Peroni, and Luigi Fabrizio Rodella. Thymus and aging: morphological, radiological, and functional overview. *Age*, 36:313–351, 2014.
- [3] AJ Freemont and JA Hoyland. Morphology, mechanisms and pathology of musculoskeletal ageing. *The Journal of Pathology: A Journal of the Pathological Society of Great Britain and Ireland*, 211(2):252–259, 2007.
- [4] Jörg J. Goronzy and Cornelia M. Weyand. The Innate and Adaptive immune systems. In *Goldman’s Cecil Medicine*, pages 214–222. W.B. Saunders, 24 edition, 2012.
- [5] Jason Gill, Mark Malin, Jayne Sutherland, Daniel Gray, George Hollander, and Richard Boyd. Thymic generation and regeneration. *Immunological Reviews*, 195(1):28–50, 2003.
- [6] Jörg J. Goronzy and Cornelia M. Weyand. Immune aging and autoimmunity. *Cellular and Molecular Life Sciences*, 69(10):1615–1623, May 2012.
- [7] J. Baran-Gale, M. D. Morgan, S. Maio, F. Dhalla, I. Calvo-Asensio, M. E. Deadman, A. E. Handel, A. Maynard, S. Chen, F. Green, R. V. Sit, N. F. Neff, S. Darmanis, W. Tan, A. P. May, J. C. Marioni, C. P. Ponting, and G. A. Holländer. Ageing compromises mouse thymus function and remodels epithelial cell differentiation. *eLife*, 9:1–27, August 2020.
- [8] Janko Nikolich-Zugich. The twilight of immunity: emerging concepts in aging of the immune system. *Nature immunology*, 19(1):10–19, 2018.
- [9] Zhanfeng Liang, Xue Dong, Zhaoqi Zhang, Qian Zhang, and Yong Zhao. Age-related thymic involution: Mechanisms and functional impact. *Aging Cell*, 21(8):e13671, 2022.
- [10] Yujun Deng, Zhengcan Peng, Kang Ming, Xiaona Qiao, Bin Ye, Yan Liu, Haiyue Wang, Peng Yang, Yu Zhang, Kun Zhou, Quanwei Huang, Wei Guo, Yi Xie, Hong Chen, Hui Yu, Liangbin Lin, Xinkai Zou, Keyue Wang, Pengbo Guan, Birong Dong, Xiaolong Chen, Xiaowen Wang, Jia Hu, Yuzhang Wu, Huiyuan Zhang, and Hongbo Hu. Single-cell analysis of human thymus and peripheral blood unveils the dynamics of T cell development and aging. *Nature Aging*, October 2025.
- [11] Yehezqel Elyahu and Alon Monsonogo. Thymus involution sets the clock of the aging t-cell landscape: Implications for declined immunity and tissue repair. *Ageing research reviews*, 65:101231, 2021.
- [12] Thomas Venables, Ann V. Griffith, Alice DeAraujo, and Howard T. Petrie. Dynamic changes in epithelial cell morphology control thymic organ size during atrophy and regeneration. *Nature Communications*, 10(1):4402, September 2019.
- [13] Lyan Abdul, Jocelyn Xu, Alexander Sotra, Abbas Chaudary, Jerry Gao, Shravanthi Rajasekar, Nicky Anvari, Hamidreza Mahyar, and Boyang Zhang. D-crypto: deep learning-based analysis of colon organoid morphology from brightfield images. *Lab on a Chip*, 22(21):4118–4128, 2022.
- [14] Felix Ambellan, Stefan Zachow, and Christoph von Tycowicz. Rigid motion invariant statistical shape modeling based on discrete fundamental forms: Data from the osteoarthritis initiative and the alzheimer’s disease neuroimaging initiative. *Medical Image Analysis*, 73:102178, 2021.
- [15] Edelsbrunner, Letscher, and Zomorodian. Topological persistence and simplification. *Discrete & computational geometry*, 28:511–533, 2002.
- [16] David Cohen-Steiner, Herbert Edelsbrunner, and John Harer. Stability of persistence diagrams. In *Proceedings of the twenty-first annual symposium on Computational geometry*, pages 263–271, 2005.
- [17] Katharine Turner, Sayan Mukherjee, and Doug M Boyer. Persistent homology transform for modeling shapes and surfaces. *Information and Inference: A Journal of the IMA*, 3(4):310–344, 2014.

- [18] Lorin Crawford, Anthea Monod, Andrew X Chen, Sayan Mukherjee, and Raúl Rabadán. Predicting clinical outcomes in glioblastoma: an application of topological and functional data analysis. *Journal of the American Statistical Association*, 115(531):1139–1150, 2020.
- [19] Henry Kirveslahti and Xiaohan Wang. Digital euler characteristic transform. *arXiv preprint arXiv:2411.08522*, 2024.
- [20] Ernst Roell and Bastian Rieck. Differentiable euler characteristic transforms for shape classification. *arXiv preprint arXiv:2310.07630*, 2023.
- [21] Pierre Schapira. Tomography of constructible functions. In *International Symposium on Applied Algebra, Algebraic Algorithms, and Error-Correcting Codes*, pages 427–435. Springer, 1995.
- [22] Justin Curry, Sayan Mukherjee, and Katharine Turner. How many directions determine a shape and other sufficiency results for two topological transforms. *Transactions of the American Mathematical Society, Series B*, 9(32):1006–1043, 2022.
- [23] Robert Ghrist, Rachel Levanger, and Huy Mai. Persistent homology and euler integral transforms. *Journal of Applied and Computational Topology*, 2:55–60, 2018.
- [24] Primoz Skraba and Katharine Turner. Wasserstein stability for persistence diagrams. *arXiv preprint arXiv:2006.16824*, 2020.
- [25] Lewis Marsh and David Beers. Stability and inference of the euler characteristic transform. *arXiv preprint arXiv:2303.13200*, 2023.
- [26] Kun Meng, Jinyu Wang, Lorin Crawford, and Ani Eloyan. Randomness of shapes and statistical inference on shapes via the smooth euler characteristic transform. *Journal of the American Statistical Association*, (just-accepted):1–25, 2024.
- [27] Bruce Wang, Timothy Sudijono, Henry Kirveslahti, Tingran Gao, Douglas M Boyer, Sayan Mukherjee, and Lorin Crawford. A statistical pipeline for identifying physical features that differentiate classes of 3d shapes. *The Annals of Applied Statistics*, 15(2):638–661, 2021.
- [28] Lewis Marsh, Felix Y Zhou, Xiao Qin, Xin Lu, Helen M Byrne, and Heather A Harrington. Detecting temporal shape changes with the euler characteristic transform. *Transactions of Mathematics and Its Applications*, 8(2):tnae002, 2024.
- [29] Jan Reininghaus, Stefan Huber, Ulrich Bauer, and Roland Kwitt. A stable multi-scale kernel for topological machine learning. In *Proceedings of the IEEE conference on computer vision and pattern recognition*, pages 4741–4748, 2015.
- [30] Genki Kusano, Yasuaki Hiraoka, and Kenji Fukumizu. Persistence weighted gaussian kernel for topological data analysis. In *International conference on machine learning*, pages 2004–2013. PMLR, 2016.
- [31] Mathieu Carriere, Marco Cuturi, and Steve Oudot. Sliced wasserstein kernel for persistence diagrams. In *International conference on machine learning*, pages 664–673. PMLR, 2017.
- [32] Rushil Anirudh, Vinay Venkataraman, Karthikeyan Natesan Ramamurthy, and Pavan Turaga. A riemannian framework for statistical analysis of topological persistence diagrams. In *Proceedings of the IEEE conference on computer vision and pattern recognition workshops*, pages 68–76, 2016.
- [33] Tam Le and Makoto Yamada. Persistence fisher kernel: A riemannian manifold kernel for persistence diagrams. *Advances in neural information processing systems*, 31, 2018.
- [34] Michael E Van Huffel, Olympio Hacquard, Vadim Lebovici, and Matteo Palo. Discrete transforms of quantized persistence diagrams. In *2025 Proceedings of the Symposium on Algorithm Engineering and Experiments (ALENEX)*, pages 68–80. SIAM, 2025.
- [35] Xiang Bai, Wenyu Liu, and Zhuowen Tu. Integrating contour and skeleton for shape classification. In *2009 IEEE 12th international conference on computer vision workshops, ICCV workshops*, pages 360–367. IEEE, 2009.

- [36] Xinggang Wang, Bin Feng, Xiang Bai, Wenyu Liu, and Longin Jan Latecki. Bag of contour fragments for robust shape classification. *Pattern recognition*, 47(6):2116–2125, 2014.
- [37] Henry Adams, Theodore Emerson, Michael Kirby, Ryan Neville, Christopher Peterson, Paul Shipman, Svetlana Chepushtanova, Eric Hanson, Francesco Motta, and Les Ziegelmeier. Persistence images: A stable vector representation of persistent homology. *Journal of Machine Learning Research*, 18(8):1–35, 2017.
- [38] Christoph D Hofer, Roland Kwitt, and Marc Niethammer. Learning representations of persistence barcodes. *Journal of Machine Learning Research*, 20(126):1–45, 2019.
- [39] Fan Wang, Hubert Wagner, and Chao Chen. Gpu computation of the euler characteristic curve for imaging data. *arXiv preprint arXiv:2203.09087*, 2022.
- [40] Ingwer Borg and Patrick JF Groenen. *Modern multidimensional scaling: Theory and applications*. Springer, 2005.
- [41] Joseph B Kruskal. Multidimensional scaling by optimizing goodness of fit to a nonmetric hypothesis. *Psychometrika*, 29(1):1–27, 1964.
- [42] Leonid V. Kantorovich. Mathematical methods of organizing and planning production. *Management Science*, 6(4):366–422, 1960. English translation of the 1939 Russian pamphlet.
- [43] Richard Ralph. MPEG-7 Core Experiment CE-Shape-1 Test Set. Available: <https://dabi.temple.edu/external/shape/MPEG7/dataset.html>, 1999. Accessed: 2025-05-23.
- [44] Tam Le, Makoto Yamada, Kenji Fukumizu, and Marco Cuturi. Tree-sliced variants of wasserstein distances. *Advances in neural information processing systems*, 32, 2019.
- [45] Vadim Lebovici, Steve Oudot, and Hugo Passe. Efficient Computation of Topological Integral Transforms. In Leo Liberti, editor, *22nd International Symposium on Experimental Algorithms (SEA 2024)*, volume 301 of *Leibniz International Proceedings in Informatics (LIPIcs)*, pages 22:1–22:19, Dagstuhl, Germany, 2024. Schloss Dagstuhl – Leibniz-Zentrum für Informatik.
- [46] Alex Krizhevsky, Ilya Sutskever, and Geoffrey E. Hinton. Imagenet classification with deep convolutional neural networks. In *Advances in Neural Information Processing Systems*, volume 25, 2012.
- [47] Alexey Dosovitskiy, Lucas Beyer, Alexander Kolesnikov, Dirk Weissenborn, Xiaohua Zhai, Thomas Unterthiner, Mostafa Dehghani, Matthias Minderer, Georg Heigold, Sylvain Gelly, Jakob Uszkoreit, and Neil Houlsby. An image is worth 16x16 words: Transformers for image recognition at scale. In *International Conference on Learning Representations*, 2020.
- [48] Mark Sandler, Andrew Howard, Menglong Zhu, Andrey Zhmoginov, and Liang-Chieh Chen. Mobilenetv2: Inverted residuals and linear bottlenecks. In *Proceedings of the IEEE Conference on Computer Vision and Pattern Recognition*, pages 4510–4520, 2018.
- [49] Mingxing Tan and Quoc V. Le. Efficientnet: Rethinking model scaling for convolutional neural networks. In *Proceedings of the 36th International Conference on Machine Learning*, pages 6105–6114, 2019.
- [50] Gábor J Székely and Maria L Rizzo. Energy statistics: A class of statistics based on distances. *Journal of statistical planning and inference*, 143(8):1249–1272, 2013.
- [51] Leonard Kaufman and Peter J Rousseeuw. *Finding groups in data: an introduction to cluster analysis*. John Wiley & Sons, 2009.
- [52] Andrea J White, Sonia M Parnell, Adam Handel, Stefano Maio, Andrea Bacon, Emilie J Cosway, Beth Lucas, Kieran D James, Jennifer E Cowan, William E Jenkinson, et al. Diversity in cortical thymic epithelial cells occurs through loss of a foxn1-dependent gene signature driven by stage-specific thymocyte cross-talk. *The Journal of Immunology*, 210(1):40–49, 2023.
- [53] Nicolas Bonneel, Julien Rabin, Gabriel Peyré, and Hanspeter Pfister. Sliced and radon wasserstein barycenters of measures. *Journal of Mathematical Imaging and Vision*, 51(1):22–45, 2015.

- [54] Peter J. Rousseeuw. Silhouettes: A graphical aid to the interpretation and validation of cluster analysis. *Journal of Computational and Applied Mathematics*, 20:53–65, 1987.
- [55] Y. Goltsev, N. Samusik, J. Kennedy-Darling, S. Bhate, M. Hale, G. Vazquez, S. Black, and G. Nolan. Deep profiling of mouse splenic architecture with codex multiplexed imaging. *Cell*, 174:968–981, 2018.
- [56] C. Stringer, T. Wang, M. Michaelos, and M. Pachitariu. Cellpose: a generalist algorithm for cellular segmentation. *Nature Methods*, 18(1):100–106, 2021.
- [57] Longin Jan Latecki, Rolf Lakämper, and Ulrich Eckhardt. Shape Descriptors for Non-Rigid Shapes with a Single Closed Contour. In *Proceedings of the IEEE Conference on Computer Vision and Pattern Recognition (CVPR)*, pages 1424–1429, 2000.
- [58] Pauli Virtanen, Ralf Gommers, Travis E. Oliphant, Matt Haberland, Tyler Reddy, et al. SciPy 1.0: Fundamental Algorithms for Scientific Computing in Python. *Nature Methods*, 17(3):261–272, 2020.
- [59] Lou van den Dries. *Tame topology and o-minimal structures*, volume 248 of *London Mathematical Society Lecture Note Series*. Cambridge University Press, Cambridge, 1998.
- [60] David G. Kendall, Dennis Barden, Timothy K. Carne, and Huiling Le. *Shape and Shape Theory*. John Wiley & Sons, Chichester, England, 1999.
- [61] David Cohen-Steiner, Herbert Edelsbrunner, John Harer, and Yuriy Mileyko. Lipschitz functions have 1 p-stable persistence. *Foundations of Computational Mathematics*, 10(2):127–139, 2010.
- [62] Paweł Dłotko and Davide Gurnari. Euler characteristic curves and profiles: a stable shape invariant for big data problems. *GigaScience*, 12:giad094, 2023.
- [63] Shreya Arya, Justin Curry, and Sayan Mukherjee. A sheaf-theoretic construction of shape space. *Foundations of Computational Mathematics*, 25(3):813–863, 2025.
- [64] V.Š. Varadarajan. On the convergence of sample probability distributions. *Sankhyā: The Indian Journal of Statistics*, 19(1/2):23–26, 1958.
- [65] Sergey Bobkov and Michel Ledoux. *One-dimensional empirical measures, order statistics, and Kantorovich transport distances*, volume 261. American Mathematical Society, 2019.
- [66] scikit-fmm developers. scikit-fmm: Fast marching methods in python. <https://github.com/scikit-fmm/scikit-fmm>, 2011. Version 0.4.2, accessed on 2025-03-26.
- [67] Fabian Pedregosa, Gaël Varoquaux, Alexandre Gramfort, Vincent Michel, Bertrand Thirion, Olivier Grisel, Mathieu Blondel, Peter Prettenhofer, Ron Weiss, Vincent Dubourg, Jake Vanderplas, Alexandre Passos, David Cournapeau, Matthieu Brucher, Marco Perrot, and Emmanuelle Duchesnay. Scikit-learn: Machine Learning in Python. *Journal of Machine Learning Research*, 12:2825–2830, 2011.
- [68] Corinna Cortes and Vladimir Vapnik. Support-vector networks. *Machine Learning*, 20(3):273–297, 1995.